Stony Brook University

Investigation of Factors that Control Droplet Formation in Microfluidic Cross-Junctions Using the Lattice Boltzmann Method

A Thesis Presented

by

Jason Pellegrino

to

The Graduate School

in Partial Fulfillment of the

Requirements

for the Degree of

Master of Science

in

Materials Science and Engineering

Stony Brook University

December 2012

Stony Brook University
The Graduate School

Jason Pellegrino

We, the thesis committee for the above candidate for the
Master of Science degree, hereby recommend
acceptance of this thesis.

Dilip Gersappe
Professor and Graduate Program Director
Materials Science and Engineering

Yizhi Meng
Associate Professor
Materials Science and Engineering

Miriam Rafailovich
Professor
Materials Science and Engineering

This thesis is accepted by the Graduate School

Charles Taber
Interim Dean of the Graduate School

An Abstract of

Investigation of Factors that Control Droplet Formation in Microfluidic Cross-Junctions Using the Lattice Boltzmann Method

by

Jason Pellegrino

Master of Science

in

Materials Science and Engineering

Stony Brook University

2012

Microfluidics could potentially provide a cheaper and more effective alternative to current industrial and laboratory fluid management techniques due to the large surface area-to-volume ratios; however, optimization of the flow conditions necessary for precise droplet generation is required for any segmented flow application. The Shan-Chen multicomponent multiphase Lattice Boltzmann method was used to simulate droplet formation conditions and provide insight about the conditions for different flow regimes like streaming, threading, and stable droplet generation. For the range of numerically stable flow conditions tested, the combined effects of the Capillary number and velocity ratio were demonstrated to be the process drivers for the cross-junction droplet size while the other dimensionless numbers had a less significant effect. Future studies include the analysis of other multiphase models to improve the numerical stability and reduce spurious velocities. In addition, there has already been some success in incorporating tracer particles into cross-junction droplets to quantify mixing during droplet coalescence. Further improvements will incorporate suspended magnetic particles to simulate the afforded mixing and separation capabilities.

Table of Contents

List of Figures

List of Tables

1. Introduction

Interest in the field of microfluidics has been growing due to the breadth of reported applications and the potential benefits for efficient and cheap analytical and industrial processes. Often, the terms "lab-on-a-chip" devices and "Micro Total Analysis Systems" (μTAS) are used as keywords because they capture the overlying goal for the field – to perform a host of laboratory operations on the micron scale in order to decrease costs and increase throughput. The cost reductions will be realized from the cheap, versatile and uniform fabrication techniques, which will produce devices with smaller footprints and smaller consumable requirements. The superior precision afforded by the associated large surface-to-volume ratios will also facilitate automated high-throughput synthesis and screening methods. The relatively large surface areas will grant improved control over the small diffusion lengths, increased exposures for surface-based assays, and predictable flow velocities for controlled mixing and interface management [1,2,3]. However, in order for such microfluidic systems to compete with current commercially available methods such as automated liquid handling systems or lateral flow strips, they will need to provide a viable alternative for certain fundamental operations such as precision fluid volume management, mixing, incubation, and indexing [3].

One of the most prevalent methods for precision management of small volumes in microchannels involves $segmented$ multiphase flow – structured droplets of one phase partition the desired components (e.g. biological entities, reagents, chemical reactions etc.) from a second immiscible carrier phase. Such methods have been documented for a wide variety of applications ranging from

inorganic nanoparticle synthesis [4,5,6], to cellular and sub-cellular mechanics and reaction kinetics [7], and to organic microreactors [8,9,10]. For example, Ahmed et al. (2006) reported that organic synthesis reactions in segmented flow microchannels had faster reaction rates as compared to reactions in homogenous (single phase) microreactors or bulk flasks [11]. They attributed the enhanced reaction rates to the suspected vortices generated within each phase of the segmented flow. A schematic of the T-junction used for their droplet generation can be seen in Figure 1. Although the T-junction configuration used to generate the drop segments is one of the simplest and most established designs, they had to optimize the microchannel geometries, sizes, and flow rates in order to achieve proper reagent addition and sufficient mixing for their particular chemical system.

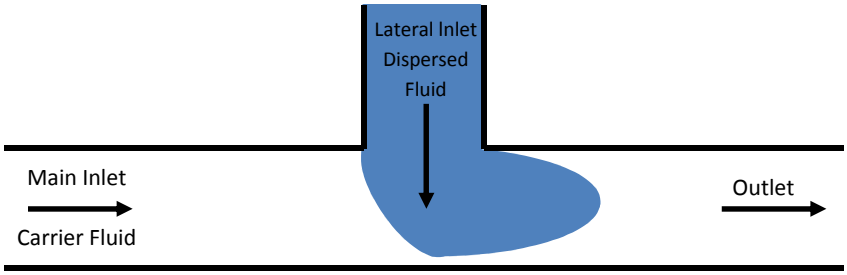

Figure 1. A schematic of the T-junction configuration used for droplet generation in reference [11].

Song et al. (2006) used segmented flow to provide precise measurements for blood-clotting times, which has clinical implications for anticoagulant drug dosing and point-of-care devices [12]. In order to provide better control for the titration of the anticoagulant into the blood droplets, they tested several microchannel designs and found that they were able to maintain the best control over the coagulation reaction with careful control of the surface tension of the microchannel walls. By introducing a hydrophobic Teflon coating to the main channel, the blood samples were encapsulated by the carrier fluid to prevent any sample adsorption to the channel walls. The novel aspect of their setup involved the addition of a hydrophilic side-channel that maintained a droplet of the titrant within the intersection until it coalesced with an incoming blood droplet. In addition to the optimization of the flow rates and

geometries, this method also required experimental determination of the proper flow conditions for droplet synchronization between the different source channels [12].

A variation of another well documented method for combining reactants in well-defined droplet segments was utilized by Liau et al (2005) to perform reactions within high-concentration biological solutions mimicking intracellular conditions [13]. While T-junctions involve the perpendicular intersection of two inlet streams and an outlet stream, cross-junction devices generally incorporate an additional inlet stream to create a four-way cross-junction. A schematic for the cross-junction configuration can be seen in Figure 2.

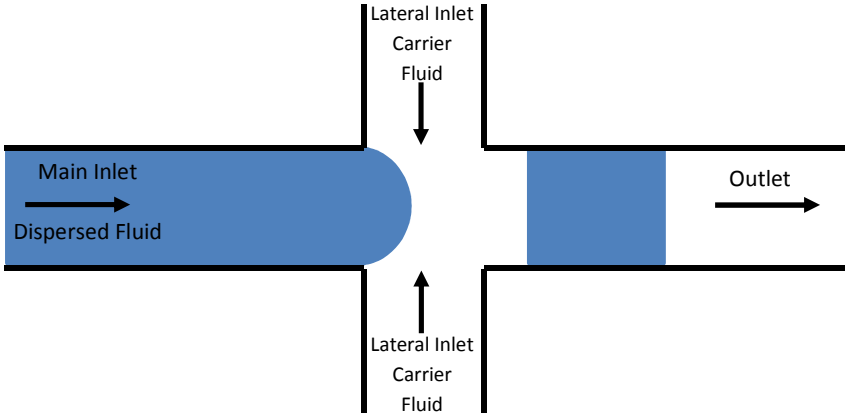

Figure 2. A schematic of the cross-junction configuration used for droplet generation in reference [13] and for the simulations described in this study.

Liau et al. (2005) found that the two symmetrically opposing streams in the cross junction reduced wall contamination, prevented swirling at the point of plug formation, and allowed them to produce smaller droplets of their highly viscous solutions [13]. What was unique about their experimental setup was that they used three converging streams to combine their reactants just prior to the droplet dispersion at the cross-junction and they experimented with protrusions on a downstream serpentine section of the capillary walls to enhance mixing within the droplets. Again, their study required experimentation

with the geometries and flow conditions in order to optimize the balance between the droplet formation mechanisms with proper reactant ratios and the downstream mixing dynamics.

An interesting variant of the cross-junction was also used to enhance a process for yet another completely different technology sector – to perform controlled CdS nanoparticle synthesis reactions. Hung et al. (2006) reported the production of smaller and more monodisperse nanoparticles as compared to conventional mixing methods [14]. In order to maintain precise control over reactant additions, they modified the cross-junction in order to alternate droplet generation between the two opposing inlets at the four-way junction. By integrating a diverging channel immediately downstream from the junction to promote drainage of the carrier fluid, they were able to dictate the fusion of the droplets from the two different reactant streams. By varying the flow conditions and the geometry, they were able to achieve different sized droplets with different ratios between the number of drops formed from each opposing inlet. However, they found that their control of the droplet sizes and ratios were limited by the conditions required for droplet coalescence [14].

While each of these segmented flow applications span a wide breadth of technology fields, they all share several core features for liquid handling; however, a better understanding of the microfluidic dynamics is required in order to extend these basic functionalities to any generic process. In particular, each of these systems requires methods for dispensing droplets with precise volumes, combining droplets or injecting components into a particular phase, and controlling the mixing of components. Without a universal method to implement all these functionalities, each microfluidic system would have to be tailor made to suit the specific application. Therefore, an understanding of the relative velocity and pressure fields for each phase would be required to predict the droplet sizes (reaction volumes), the conditions for droplet coalescence, the rates for reagent injection into a plug, and the mixing/reaction kinetics for a particular chemical system. Because even the more fundamental microfluidic operations

are governed by a large set of experimental parameters and involve complex geometries/flow-fields, numerical simulations are often required to fill in the gaps between modern empirical and theoretical analyses. With so many considerations for the design of a custom microfluidic system, the predictions from numerical simulations provide valuable savings from excessive costs during empirical investigation, especially when dealing with expensive reagents. In addition, numerical simulations not only supplement empirical testing and theory but also provide a medium in which new ideas can be tested for which there are no current techniques.

The Lattice Boltzmann Method (LBM) is a suitable technique for predicting microfluidic flows because it can calculate complex dynamics and geometries on a "mesoscopic" scale [15]. While traditional computational fluid dynamics approaches involve the calculation of the macroscopic conservation equations in discrete space, they often experience difficulties when trying to implement features arising from microscopic origins like surface wetting or interfacial slip [16]. Furthermore, the traditional macroscopic multiphase flow simulations can become computationally demanding as they require additional algorithms to track the moving interfaces and prevent the surface discontinuity from becoming smoothed-out during the iterative averaging process [17,18, 19]. On the other hand, molecular dynamics approaches easily incorporate micro-scale behaviors because they track the evolution of individual molecules with interaction potentials. However, such microscopic methods are even more computationally demanding as each molecule has at least six degrees of freedom – three spatial components and three velocity components. Therefore, molecular dynamic simulations are usually limited to small number of molecules tracked over a small number of time increments [16, 20]. Finally, the LBM acts as a compromise between the macroscopic and microscopic dynamics because it tracks the evolution of fictitious packets of fluid as particle distribution functions, which eliminates the need for statistical averaging of the molecular fluctuations and allows facile recovery of the macroscopic

variables of interest. In addition, one of the pillars of LBM is that the dynamics are based on the concept of "relaxation towards local equilibrium," which allows each fluid node to be solved independently making the method very efficient with parallel processing. Further details for the local equilibrium paradigm and the LBM theory will be discussed in the following section.

2. Lattice Boltzmann Theory

2.1 Streaming and Space Discretization

In order to understand how the evolution of these abstract fluid packets provides insight for complex fluid flows, it is necessary to understand how space and time are discretized in the Lattice Boltzmann (LB) method. In lattice based methods, space is discretized into regularly distributed nodes each containing a particle population for each of the vectors that connect neighboring nodes. For each iteration of the simulation, the particle populations are passed between each neighboring nodes according to the predefined vectors that connect them – this passing of information is called the streaming step. Therefore, if one focuses on a particular node, it acts as a central hub to calculate the interaction of all the particles entering that point in space from the adjacent nodes. Figure 3 provides a schematic for the lattice with eight nearest neighbors used in this study. It has been dubbed the D2Q9 lattice because it is two-dimensional and contains nine particle populations per node (a population that travels to/from each of the eight nearest neighbors and a population that stays at the node). There can be many choices for the structure of the lattice; however, the D2Q9 model has been used extensively for two-dimensional simulations because it provides sufficient symmetry to recover the desired partial differential equations (e.g. Navier-Stokes equation for incompressible flows) with second order approximation accuracy and because the square unit cells are amenable to the array indexing typically used for computer data structures [21, 22].

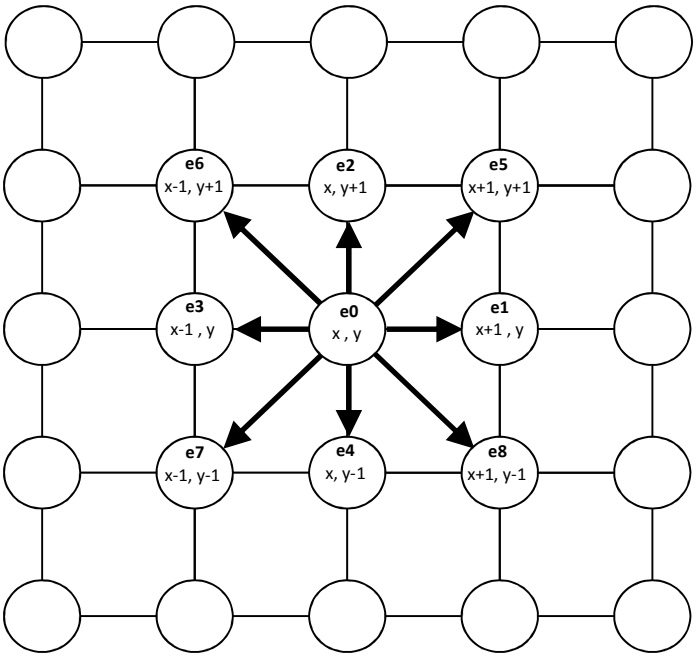

Figure 3. Schematic of the D2Q9 lattice used throughout this study. There are 8 vectors that connect each node to its nearest neighbors - 4 vectors with magnitude 1 $\frac{lu}{ts}$, 4 vectors with magnitude $\sqrt{2}\,\frac{lu}{ts}$, and a ninth vector with zero magnitude that retains particles at the node.

While space is segregated into regular nodes, time is broken into evenly spaced intervals according to each iteration of particle interaction calculations across the entire lattice. In other words, at each time step, a calculation of the momentum change from the "collision" between all the impinging fluid particles is performed and hence the need for Boltzmann's mathematical description of kinetic theory.

2.2 Kinetic theory and Maxwell-Boltzmann Distribution

The Boltzmann Equation was established to provide a mathematical description of the macroscopic observable quantities for gasses based on a statistical analysis of the underlying microscopic behavior. By treating the gas molecules like hard spheres undergoing inelastic collisions, Boltzmann was able to

employ classical mechanics to describe quantities like temperature and pressure in terms of the number, mass, and velocity of gas molecules [23]. In order to describe the transient motions of such a large number of molecules (at least the order of Avogadro's number, 10^{23}), Boltzmann considered the evolution of a probability density function rather than tracking the motions of the individual molecules. Consider a system with just one particle. At any particular instant in time, the function $f(\vec{x}, \overrightarrow{p}, t)d\vec{x}d\vec{p}$ would describe the probability of finding a molecule or fluid packet within a particular region of space, $\vec{x} \pm d\vec{x}$, with momentum in the range $d\vec{p}$ about $\vec{p}$. If one were to add $N-1$ particles to the system, each of these particles would have the opportunity to interact, and therefore we would require $f^{(N)}(\vec{x}, \overrightarrow{p}, t)$ distribution functions to describe the effects of the N-body system on one another [15, 23]. Although there would be just as many possible distribution functions as there are particles in the system, Boltzmann focused on the one-body distribution function through the assumption of "molecular chaos" – the particles spend most of the time in free trajectories and only interact over very minute time-periods from short-range two-body potentials [15]. With a large number of molecules undergoing such chaotic motion, one molecule cannot be distinguished from another, and therefore the one-body distribution function could be used to describe the probability distribution for the choice of any one molecule. This assumption gains validity for phenomena that can be characterized by small Knudsen numbers – a number that describes the ratio between the typical distance the molecules have to span before experiencing a collision ($l_{mean\ free\ path}$) and the characteristic distance that defines macroscopic gradients ($l_{characterstic}$):

$$Kn = \frac{l_{mfp}}{l_c}. \tag{2.1}$$

Given the set of initial conditions for the one-body distribution function with no intermolecular collisions, one would be able to describe the location and velocity of the particles for all time points

because they would stream along their initial trajectories. Thus, over the course of some time interval, Δt, the probability distribution function for particles with mass, m, would evolve according to:

$$f(\vec{x} + \vec{p}/m\,\Delta t, \vec{p}, t + \Delta t) - f(\vec{x}, \vec{p}, t) = 0. \tag{2.2}$$

Without collisions, there would be no change in the velocity distribution over time and the particles would just change in their positions. This represents the streaming process – knowledge of the velocity distribution in space allows one to predict the trajectories of the particles. However, if two-particles were to collide, the transfer of momentum would alter the particles' trajectories and the resulting distribution functions. Therefore, Boltzmann defined the collision operator as the differential change in the distribution function as a result of these two body interactions and an arbitrary external force, $\vec{F}$.

$$f\left(\vec{x} + \vec{p}/m \cdot \Delta t, \vec{p} + \vec{F} \cdot \Delta t, t + \Delta t\right) - f(\vec{x}, \vec{p}, t) = \Omega(f)\Delta t \tag{2.3}$$

$$\Omega(f) = \lim_{\Delta t \to 0} \left(\frac{f\left(\vec{x} + \vec{p}/m \cdot \Delta t, \vec{p} + \vec{F}\Delta t, t + \Delta t\right) - f(\vec{x}, \vec{p}, t)}{\Delta t} \right) = \left[\partial_t + \vec{p}/m \cdot \partial_{\vec{x}} + \vec{F}\partial_{\vec{p}}\right] f(\vec{x}, \vec{p}, t)$$

The convenient implementation of this collision operator is one of the critical features that makes LBM so versatile and computationally efficient with parallel computing. The local (independent from neighboring nodes) implementation of the collision operator allows for different domains of the lattice to be divvied among multiple processors so that the calculations are performed resourcefully. In order to provide insight into the local operations of each node, one must begin with the concept of local equilibrium – the case when the collision operator has no impact on the distribution functions. As a result of particle collisions, some of the particles starting from position $\vec{x}$ will not stream to the position $\vec{x} + \vec{p}/m \cdot dt$ (loss of particles), and some particles from other positions will undergo collisions that cause them to arrive at $\vec{x} + \vec{p}/m \cdot dt$ (gain of particles) [22]. Therefore, local equilibrium occurs when the collision operator is rendered inconsequential from perfectly balanced particle gains and losses.

From the assumption of molecular chaos, the balance between the particle gains and losses from collisions can be described by the one-body distribution functions that fit the form:

$$\underbrace{f_1' f_2'}_{\text{Gains from Inverse Collision}} = \underbrace{f_1 f_2}_{\text{Losses from Direct Collision}} \tag{2.4}$$

where the f' distributions represent the inverse collision that lead to particle gains and the numeral subscripts demark the two different particle populations experiencing the collision [15]. Taking the logarithm of both sides reveals that the local equilibrium distribution function, ln f^{eq}, is an additive collision invariant, which provides insight to the functional form and the necessary parameters. Since the equilibrium distribution function remains constant for all collision processes, it should only depend on the properties such as mass, momentum, and energy that are conserved for any collision event. Therefore, the additive nature of ln f^{eq} suggested the form:

$$f^{eq} = e^{(A + B_a v_a + \frac{1}{2} C v^2)} \tag{2.5}$$

where A, B_a, and C are five Lagrangian multipliers that represent the dependence on the conserved hydrodynamic fields and v_a is the Cartesian components of the particle velocity vector, $\vec{v}$, for a = 1,2 in two dimensions [15]. Because the mass, momentum, and energy are conserved by definition of the moments of the distribution functions, they are applied to solve for the unknown coefficients:

$$\text{Mass:} \qquad \rho(\vec{x}, t) = m \int f(\vec{x}, \vec{v}, t) d\vec{v}$$

$$\text{Momentum:} \qquad \rho(\vec{x}, t) \cdot u(\vec{x}, t) = m \int \vec{v} \cdot f(\vec{x}, \vec{v}, t) d\vec{v} \tag{2.6}$$

Energy: $$\rho e(\vec{x},t) = \frac{m}{2}\int(\vec{v}^2 \cdot f(\vec{x},\vec{v},t)d\vec{v}$$

where ρ is the macroscopic fluid density (mass per unit volume), $\vec{u}$ is the macroscopic flow velocity, and ρe is the energy density. As a result, we arrive at the well-established Maxwell-Boltzmann distribution for D spatial dimensions [24]:

$$f^{eq} = \rho \left(\frac{m}{2\pi kT}\right)^{\frac{D}{2}} \cdot e^{\left(\frac{-mv^2}{2kT}\right)} \tag{2.7}$$

where k is Boltzmann's constant, and T is the macroscopic temperature for the collection of gas molecules. Although this distribution describes the condition for local equilibrium, it does not mean that flow velocities and temperatures have achieved steady state – the physical interpretation for local equilibrium become more tangible upon analysis of the different time scales for the fluid particle interactions. The relaxation to local equilibrium involves the smoothing of the erratic molecular velocities into a continuous distribution function, which occurs at a must faster time scale compared to global equilibration [15].

2.3 Discrete Collisions

In order to apply the notion of local equilibrium to the numerical approximations of the Lattice Boltzmann method, a suitable method for discretizing the distribution functions according to the lattice structure is required to preserve the desired hydrodynamics. Even with the molecular chaos assumptions, the two-body collisions still involve non-linear integral calculations; therefore, further simplifications were made to facilitate numerical methods. The monumental paper by Bhatnagar, Gross,

and Krook, suggested a suitable approximation for the collision operator in which the distribution functions undergo a linear relaxation towards local equilibrium according to [25]:

$$\Omega^{BGK} = -\frac{f - f^{eq}}{\tau} = -\omega\,(f_i - f_i^{eq}) \tag{2.8}$$

where τ is the relaxation time, ω is the collision frequency (inverse of the relaxation time) used for numerical calculations, and the i subscript indexes each of the discrete lattice velocities for $i = 0 \cdots q - 1$ ($q = 9$ for the D2Q9 lattice used in the present study). In order for the macroscopic variables, represented by the moments of the distribution functions, and the equilibrium distribution function to translate into the discrete lattice space, the functions have to be weighted according to the different lattice velocity magnitudes. For example, in the D2Q9 model, there are three different lattice velocities, $\overrightarrow{c_i}$, associated with each node: the "rest" velocity, $\overrightarrow{c_0}$, has zero velocity as it does not stream any information to the neighboring nodes, $\overrightarrow{c_1}$ through $\overrightarrow{c_4}$ have magnitudes of 1 lattice unit per time-step $\left(\frac{lu}{ts}\right)$ because they stream to the adjacent nodes along the directions parallel to the axes of the lattice, and $\overrightarrow{c_5}$ through $\overrightarrow{c_8}$ have magnitudes of $\sqrt{2}\,\frac{lu}{ts}$ because they stream in the direction along the diagonal hypotenuse of the isosceles right triangle formed by the lattice axes. In order to recover the conservation laws in discrete space, the moments are weighted according to the velocity magnitude using the Gauss-Hermite quadrature [26]:

$$I = \sum_{i=0}^{q-1} \psi(\overrightarrow{c_i})\, t_i\, f\,(\overrightarrow{x}, \overrightarrow{c_i}, t) \tag{2.9}$$

where $\psi(\overrightarrow{c_i})$ is a polynomial of $\overrightarrow{c_i}$ depending on the moment order, and t_i are the weighting constants that scale the distributions according to their magnitude. Therefore, the moments become [26]:

$$\rho(\vec{x},t) = \sum_{i=0}^{q-1} f_i$$

$$\rho\vec{u}(\vec{x},t) = \sum_{i=0}^{q-1} \vec{c_i} f_i \tag{2.10}$$

$$\rho e(\vec{x},t) = \frac{1}{2}\sum_{i=0}^{q-1} \vec{c_i}^2 f_i$$

where f_i is the dimensionless directionally weighted distribution function.

The directional weighting constants are calculated through the preservation of the equilibrium function. Since the speed of sound is a measureable property of the lattice and is the characteristic velocity for the dimensionless Mach number formulation, it can be related to the characteristic speed for the gas molecules of the of the equilibrium Maxwell-Boltzmann distribution at a known temperature according to [26]:

$$c_s^2 = \frac{kT}{m} = RT \tag{2.11}$$

where c_s is the speed of sound in the lattice, and R is the universal gas constant. Typically, the speed of sound is measured by introducing a density perturbation within the lattice and measuring the number of time steps it takes to propagate over a known distance. The speed of sound is another lattice dependent property as its value is subject to the choice of weighting constant for the rest particle – conversion of streamed particles into rest particles during the local equilibration impedes the propagation density perturbations. Substituting the above relation for the speed of sound (Equation 2.11) into the equilibrium Maxwell-Boltzmann distribution (Equation 2.7) and using the Taylor series expansion of $\exp\left[-\frac{\vec{u}^2 - 2\vec{u}\cdot\vec{c}}{2\,c_s^2}\right]$ one gets [26]:

$$f^{eq} = \frac{\rho}{2\pi kT} \cdot \exp\left[-\frac{\vec{c}^2}{2c_s^2}\right]\left[1 - \frac{\vec{u}^2}{2\,c_s^2} + \frac{\vec{u}\cdot\vec{c}}{c_s^2} + \frac{(\vec{u}\cdot\vec{c})^2}{2c_s^4}\right] + \vartheta(\vec{u}^3) \tag{2.12}$$

By inserting this equation into the third order Hermite polynomial for Gaussian quadrature with:

$$\psi(\vec{c}\,) = c_x^m c_y^n \tag{2.13}$$

where c_x and c_y refer to the Cartesian components of the particle velocity, and the exponents m, n refer to the moment order weight function and the number of different weight constants used to define the quadrature, the result is:

$$f^{eq} = \rho t_i\left[1 - \frac{\vec{u}^2}{2\,c_s^2} + \frac{\vec{u}\cdot\vec{c}}{c_s^2} + \frac{(\vec{u}\cdot\vec{c})^2}{2c_s^4}\right] \tag{2.14}$$

with the following weighting constants [26]:

$$t_i = \begin{cases} \frac{4}{9}\ for\ i = 0 \\ \frac{1}{9}\ for\ i = 1 \cdots 4 \\ \frac{1}{36}\ for\ i = 5 \cdots 8 \end{cases} \tag{2.15}$$

Because the dimensionless formulation of the simulation captures the magnitudes of the relative physical phenomena, the physical properties, like the magnitudes of the velocity vectors and forces, should not depend on the choice of coordinate system and should therefore be unaffected by translational and rotational transformations. This choice of weightings is sufficient because it ensures translational (Galilean) and rotational invariance and results the following relation for the D2Q9 lattice speed of sound [27]:

$$c_s^2 = \frac{c}{3} \tag{2.16}$$

where $c = 1\frac{lu}{ts}$ for the present investigation. With a complete description of the lattice and the collision process, the discrete Boltzmann equation becomes:

$$f(\vec{x} + \vec{c_i}\Delta t, t + \Delta t) - f(\vec{x}, t) = -\omega (f_i - f_i^{eq}) \quad (2.17)$$

2.4 Boundary Conditions

While the rules for information transfer between the lattice nodes have been established through the collision and streaming operators, boundaries require certain exceptions to these rules. When a node that experiences the collisions from fluid particles is at the edge of the lattice or adjacent to a non-fluid node, that node misses some of the particle distributions that should have streamed from the edge or the non-fluid node. Therefore, a different set of dynamics is implemented at the boundaries to account for the missing information. While there are several different types of boundary conditions with different methods of implementation reported in the literature, the boundary conditions can be grouped into two general categories: open and closed boundaries. For open boundaries, the fluid particles are free to stream across the artificial boundary, while for closed boundaries, there is no mass flux in the direction normal to the boundary. In the present study, Dirichlet conditions are used for open boundaries, and no-slip conditions are used for the closed boundaries.

2.4.1 No-Slip Boundary Conditions

The most widely used boundary condition for the interface between a liquid and a solid surface is the no-slip condition, which implies that the fluid velocity relative to the wall is zero [28]. Consider

the fluid node [x,y] adjacent so the solid boundary in Figure 4. In order to induce a zero velocity condition between [x,y] and the nearest neighbor solid nodes [x-1, y+1], [x-1, y], and [x-1, y-1], one would only need to determine the appropriate values for the populations f_1, f_5, and f_8 that would stream in from solid boundary because all the other populations would come from the naturally evolving adjacent fluid nodes. Note that the adjacent nodes in Figure 4 are labeled with the opposite f_i's compared to Figure 3 because the vectors are pointed towards the node of interest. In addition to these unspecified populations, the fluid node [x,y] adjacent to the boundary would also be losing the f_3, f_6, and f_7 populations that would stream out of the fluid domain. The local velocity is the sum of all the directional distribution functions at a point in space; therefore, the simplest way to annihilate the sum of the populations that traverse the boundary is to have the flux of populations entering the fluid domain diametrically oppose the flux of population leaving the domain.

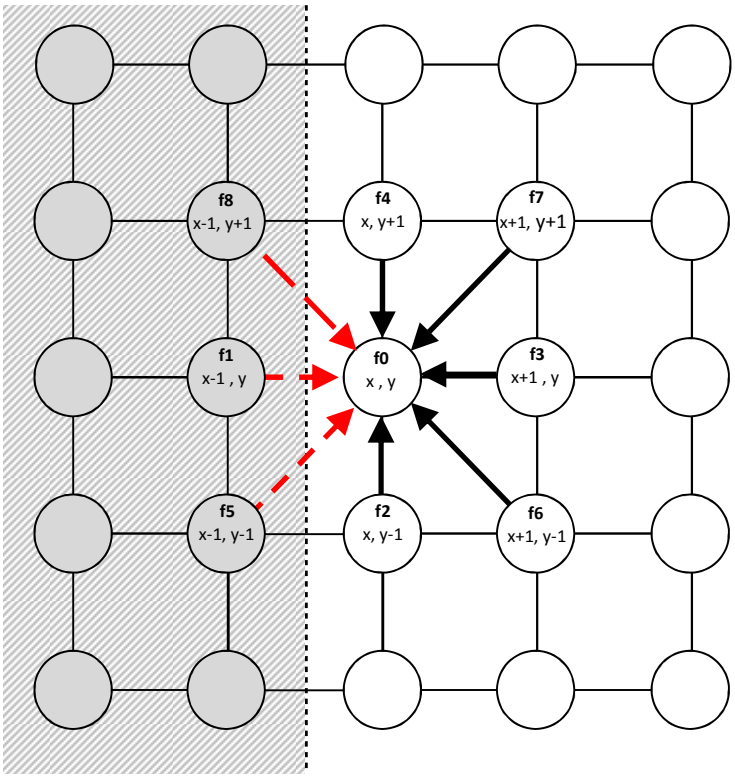

Figure 4. A representation of the missing particle populations that need to be solved for at a bounce-back boundary with a normal vector pointing in the positive x-direction. The grey, hatched-out nodes represent the bounce-back nodes of the solid boundary, and the white, unfilled nodes represent the fluid nodes that undergo typical BGK dynamics.

As a result, the most popular no-slip boundary method became known as the bounce-back method because the probability densities leaving the fluid domain are reversed in orientation back into domain. Referring back to the orientation in Figure 4, the bounce-back scheme employed throughout this investigation allowed the fluid nodes adjacent to the boundaries to collide and stream the f_3, f_6, and $f_7$populations to the bounce-back nodes; however, the bounce-back nodes would undergo a different set of dynamics. While the fluid nodes are undergoing the collision step, the bounce-back nodes just copy the values from the incoming populations to the outgoing populations with the opposite orientation according to:

$$\begin{aligned} f_{1,[x-1,y],t+1} &= f_{3,[x,y],t} \\ f_{5,[x-1,y-1],t+1} &= f_{7,[x,y],t} \\ f_{8,[x-1,y+1],t+1} &= f_{6,[x,y],t} \end{aligned} \tag{2.18}$$

Therefore, the populations that are bounced-back are involved in the fluid node collisions at the subsequent time step. Since the lattice velocity is $1\ \frac{lu}{ts}$, the velocity components can be calculated from the components of the lattice vectors according to:

$$\rho u_\alpha = \sum_{i=0}^{8} e_{i\alpha} f_i = 0 \tag{2.19}$$

where $e_{i\alpha}$ is the Cartesian component ($\alpha = x, y$) of the velocity vector defined in Table 1 according to the D2Q9 lattice depicted in Figure 3 above.

Table 1. Velocity vector components for the nine vectors of the D2Q9 model

	$\overrightarrow{e_o}$	$\overrightarrow{e_1}$	$\overrightarrow{e_2}$	$\overrightarrow{e_3}$	$\overrightarrow{e_4}$	$\overrightarrow{e_5}$	$\overrightarrow{e_6}$	$\overrightarrow{e_7}$	$\overrightarrow{e_8}$
$e_{i,x}$	0	1	0	-1	0	1	-1	-1	1
$e_{i,y}$	0	0	1	0	-1	1	1	-1	-1

As a result, the velocity at the boundary interface is annihilated according to:

$$u_x = \frac{1}{\rho}(f_1 + f_5 + f_8 - f_3 - f_6 - f_7) = 0 \tag{2.20}$$

$$u_y = \frac{1}{\rho}(f_2 + f_5 + f_6 - f_4 - f_7 - f_8) = f_2 - f_4 = 0$$

Since the flux is annihilated during the streaming phase between time-steps, the location of the no-slip boundary is considered to be at the mid-way plane between the solid and fluid nodes, which has been demonstrated to produce second-order accuracy [15].

2.4.2 Dirichlet Boundary Conditions

In the literature, flows within the microchannels are typically driven using syringe pumps that generate constant volumetric flows. Since the flow profiles are generally fully-developed or steady-state by the time the fluid reaches the junctions due to the relatively low velocities, this paper does not consider any entry effects - the simulation domain captures only the space where the phenomena of interest occur (e.g. droplet generation). Because the lattice artificially terminates at locations along the microchannels where steady flow is assumed to have been achieved, a “steady-state” fluid velocity or pressure was imposed at the open boundaries.

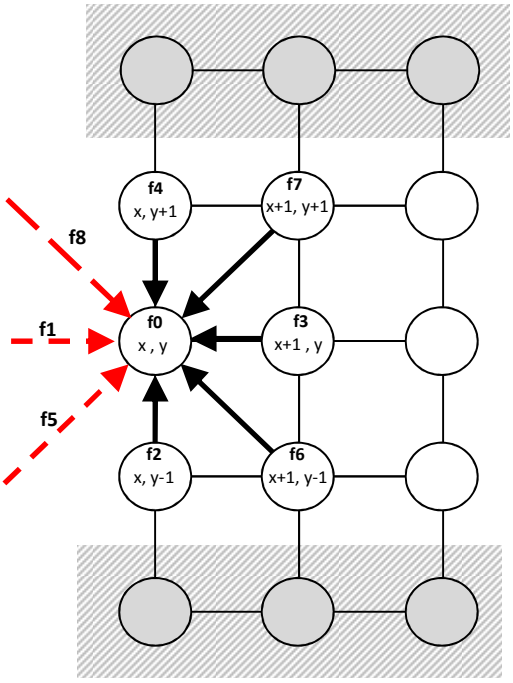

Figure 5. A representation of the missing particle populations (red vectors) that need to be solved for at a Zou-He Dirichlet open boundary with a normal vector pointing in the positive x-direction. The grey, hatched-out nodes represent the bounce-back nodes an arbitrary solid boundary

Zhou and He devised a method for imposing Dirichlet boundary conditions – a set of conditions for the particle distributions missing from the lattice edge that ensure a constant values for the macroscopic velocities or pressures [29]. First, Zou and He identified that the edge of the D2Q9 lattice presents four unknown quantities (Figure 5): the f_1, f_5, f_8 populations from the missing nodes at the lattice edge, and only one of the macroscopic moments that is the sum of the unknown populations. In order provide closure to the problem with a system of four equations, they made two key assumptions: the velocity component tangent to the boundary is null and the non-equilibrium portions of the distribution functions normal to the boundary cancel out.

For the inlet boundaries, a constant pressure value say, ρ_{in}, was imposed. Rearranging the first line of Equation 2.10 so that the unknown populations are on the left-hand side one gets:

$$f_1 + f_5 + f_8 = \rho_{in} - (f_0 + f_2 + f_3 + f_4 + f_6 + f_7) \tag{2.21}$$

For the simulations in this paper, it is safe to assume that the y-component of the inlet velocity is zero since the upstream fluid should develop Poisuelle flow.

Therefore,

$$f_2 - f_4 + f_5 + f_6 - f_7 - f_8 = 0 \tag{2.21}$$

or

$$f_5 - f_8 = f_4 - f_2 - f_6 + f_7 \tag{2.22}$$

The last unknown is the x-component of the velocity moment, u_x, which can be defined in a similar manner from the second line of Equation 2.10:

$$\rho_{in} u_x = f_1 - f_3 + f_5 - f_6 - f_7 + f_8 \tag{2.23}$$

or

$$f_1 + f_5 + f_8 = \rho_{in} u_x + f_3 + f_6 + f_7 \tag{2.24}$$

Setting the equations for the unknowns distribution functions in Equations 2.21 and 2.24 equal, we can solve for the unknown velocity moment [29].

$$\vec{u}(\vec{x}, t) = \left[\; 1 - \frac{[f_0 + f_2 + f_4 + 2(f_3 + f_6 + f_7)]}{\rho_{in}} \; , \qquad 0 \; \right] \tag{2.25}$$

To solve for the unknown distribution functions, Zou and He made the assumption that:

$$f_1 - f_1^{eq} = f_3 - f_3^{eq} \tag{2.26}$$

Or

$$f_1 = f_3 + \left(f_1^{eq} - f_3^{eq} \right) \tag{2.27}$$

The annihilation of the non-equilibrium particle fluxes seems like a reasonable assumption considering the imposed steady-state boundary density. Substituting Equation 2.14 for the equilibrium distributions, one solves for the first unknown distribution function:

$$f_1 = f_3 + \frac{2}{3}\rho_{in}u_x \tag{2.28}$$

To solve for f_5, the expression for the zero velocity y-component (Equation 2.22) is solved for f_8:

$$f_8 = f_5 - f_4 + f_2 + f_6 - f_7 \tag{2.29}$$

This expression, along with the expression for f_1 is substituted into the Equation 2.23:

$$\begin{aligned}
\rho_{in}u_x &= \left(f_3 + \frac{2}{3}\rho_{in}u_x\right) - f_3 + f_5 - f_6 - f_7 + (f_5 - f_4 + f_2 + f_6 - f_7) \\
\rho_{in}u_x &= \frac{2}{3}\rho_{in}u_x + 2f_5 - 2f_7 - f_4 + f_2 \\
f_5 &= f_7 + \frac{1}{2}(f_4 - f_2) + \frac{1}{6}\rho_{in}u_x
\end{aligned} \tag{2.30}$$

The distribution function, f_8, is solved in a similar fashion:

$$\begin{aligned}
f_7 &= f_5 - f_4 + f_2 + f_6 - f_8 \\
\rho_{in}u_x &= \left(f_3 + \frac{2}{3}\rho_{in}u_x\right) - f_3 + f_5 - f_6 - (f_5 - f_4 + f_2 + f_6 - f_8) + f_8 \\
\rho_{in}u_x &= \frac{2}{3}\rho_{in}u_x - 2f_6 + 2f_8 + f_4 - f_2 \\
f_8 &= f_6 + \frac{1}{2}(f_2 - f_4) + \frac{1}{6}\rho_{in}u_x
\end{aligned} \tag{2.31}$$

The application of the constant velocity Dirichlet boundary conditions follows an identical formulation with the same assumptions; however, in this scenario, one of the velocity components is imposed while the expression for the density is derived. Thus, they produce identical relations.

2.5 Shan-Chen Multicomponent Multiphase Dynamics

The LBM was chosen to model the segmented microfluidic flows because of the simplicity, efficiency, and versatility of the multiphase models. There are several different LBM multiphase schemes reported throughout the literature including the color gradient model [30], the free energy model [31], and the Shan-Chen model [32]. While each of these methods has advantages and disadvantages depending on the application, the Shan-Chen model was employed in this study because it has been well established in the literature for modeling capillary flows where surface tension phenomena are critical [33,34,35]. In addition, the model is easily implemented with parallel processing through the addition of a force term that preserves the local nature of the dynamics. The austerity of the model also allows for additional couplings with tracer scalars or particle suspension. However, the biggest drawback with the method is the occurrence of artificial velocities at the fluid interfaces, which will be addressed later in the discussion.

For the two-component model, two lattices are defined for the entire simulation domain, one for each of the components. Each lattice obeys the discrete Boltzmann equation for streaming and collisions [32]:

$$f_i^{\sigma}(\vec{\mathrm{x}} + \vec{\mathrm{c}_i}\Delta t, t + \Delta t) = f_i^{\sigma}(\vec{\mathrm{x}}, t) - \omega_{\sigma}\left[f_i^{\sigma}(\vec{x}, t) - f_i^{\sigma,eq}(\vec{\mathrm{x}}, t)\right] \tag{2.32}$$

where the σ superscript indexes the distribution functions for each component ($\sigma = 2$ for the present case) and each lattice has its own respective relaxation parameter. Similarly, the moments are distinguished for each lattice to calculate the density and velocity for each respective fluid. However, there is a slight modification to the equilibrium distribution to account for fluid-fluid and solid-fluid interactions. An interaction potential is introduced through the equilibrium velocity term that generates a repulsive force at the interface between the two components [32]:

$$f_i^{\sigma,eq}(\vec{\mathrm{x}},t) = t_i\rho_\sigma\left[1+\frac{\vec{\mathrm{c}_i}\cdot\vec{\mathrm{u}}_\sigma^{eq}}{c_s^2}+\frac{\left(\vec{\mathrm{c}_i}\cdot\vec{\mathrm{u}}_\sigma^{eq}\right)^2}{2c_s^4}-\frac{\vec{\mathrm{u}}_\sigma^{eq\,2}}{2c_s^2}\right] \tag{2.33}$$

The new equilibrium velocity, $\vec{\mathrm{u}}_\sigma^{eq}$, represents the common velocity modified by the force term:

$$\vec{\mathrm{u}}_\sigma^{eq} = \vec{\mathrm{u}}' + \frac{\vec{\mathrm{F}}_\sigma}{\omega_\sigma\rho_\sigma} \tag{2.34}$$

with the velocities from both lattices averaged according to:

$$\vec{\mathrm{u}}' = \frac{\sum_\sigma \omega_\sigma\rho_\sigma\vec{\mathrm{u}}_\sigma}{\sum_\sigma \omega_\sigma\rho_\sigma} \tag{2.35}$$

It is important to point out that there are three different contributions to the force term, $\vec{\mathrm{F}}_\sigma$, in the scope of this investigation: the liquid-liquid cohesive force, the solid-liquid adhesion force, and the body force (e.g. buoyancy forces or gravity) where:

$$\vec{\mathrm{F}}_\sigma = \vec{\mathrm{F}}_\sigma^{cohesion} + \vec{\mathrm{F}}_\sigma^{adhesion} + \vec{\mathrm{F}}_\sigma^{body} \tag{2.36}$$

The cohesive force is calculated according to:

$$\vec{\mathrm{F}}_\sigma^{cohesion}(\vec{\mathrm{x}},t) = -\rho_\sigma(\vec{\mathrm{x}},t)\; G\sum_i t_i\rho_{\bar{\sigma}}(\vec{\mathrm{x}}+\vec{\mathrm{c}}_i\Delta t)\vec{\mathrm{c}}_i \tag{2.37}$$

where G represents the fluid-fluid interaction parameter and the ρ_σ versus $\rho_{\bar{\sigma}}$ represents the distinction between density of the fluid experiencing the force from the density of a different fluid component. The interaction parameter is important because it provides some flexibility in adjusting the interfacial surface tension between the two fluids. To provide some insight into the mechanism of the fluid-fluid coupling, consider the hypothetical case of a flat fluid-fluid interface with a normal vector pointing in the positive x-direction in Figure 6. If the densities for both fluids are equal to unity on either side of the interface (containing zero dissolved density of the opposing component), and the interface is infinitely thin, then the nodes adjacent to the interface would experience:

$$\vec{F}_c^{cohesion} = (-\frac{G}{6}, 0) \tag{2.38}$$

$$\vec{F}_d^{cohesion} = (\frac{G}{6}, 0)$$

Thus both fluids would experience a force oriented towards their own respective fluid. However, this force term does not act as a cohesive force in the classical sense because its magnitude depends on the distance away from the interface. If you now consider fluid molecules in the body of the fluid away from the interface in the previous example, the sum of the weighted opposing densities, and thus the cohesive force, would now be zero. Opposed to the classical notion of cohesive force arising from intermolecular attractions (such as van der Waals forces), the Shan-Chan force potential is considered to have a repulsive nature because it only forces fluids away from the interface – akin to hydrophobic interactions.

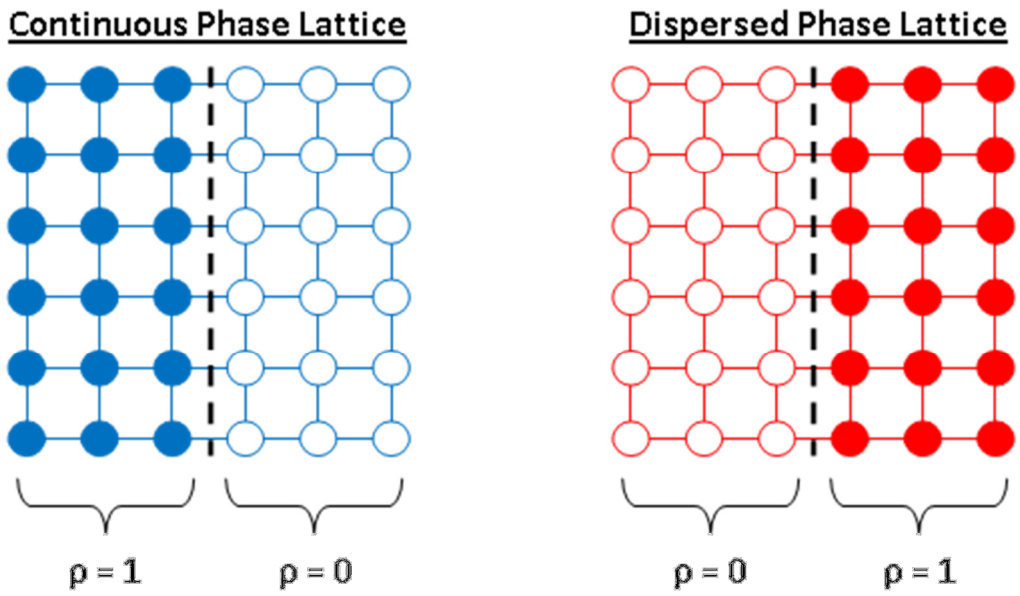

Figure 6. Representation of an ideal interface in the Shan-Chen multicomponent, multiphase lattice coupling. This is only a hypothetical situation since the Shan-Chen model typically cannot exclude all density of one phase from another. In addition, there is usually a finite thickness of the interface where the transition from high to low density spans across several lattice units

The adhesion force can be calculated in a similar fashion:

$$\vec{\mathrm{F}}_{\sigma}^{adhesion}(\vec{\mathrm{x}},t) = -\rho_{\sigma}(\vec{\mathrm{x}},t)\, G \sum_{i} t_i \rho_{wall,\bar{\sigma}}(\vec{\mathrm{x}} + \vec{\mathrm{c}}_i \Delta t)\vec{\mathrm{c}}_i \tag{2.39}$$

where ρ_{wall} is an artificial density attributed explicitly to the bounce-back nodes solely for the manipulation of the solid-fluid surface tension – this density is not used in any of the collision or streaming dynamics. This method provides an easy and effective alternative to the method commonly described in the literature, which requires building a sub-routine that checks for presence of adjacent bounce-back nodes in order to apply a separate force calculation because the typical bounce-back nodes have no meaningful density.

The dynamics of the Shan-Chen LBM can be verified through the use of the Chapman-Enskog expansion. In order to relate the collision and streaming evolutions to the established partial differential equations like the Navier-Stokes equation, perturbation theory is utilized to separate the events that occur on different timescales. For example, the particle level relaxation to local equilibrium occurs over shorter time scales as compared to the macroscopic gradient smoothing for global equilibrium. Therefore, the distribution function and the space/time derivatives are expanded to different orders of ε, a sufficiently small parameter that is usually interpreted as the Knudsen number because it is necessarily small in order for Boltzmann's molecular chaos assumption to hold [27]:

$$\begin{aligned} f_i &= f_i^{(0)} + \varepsilon f_i^{(1)} + \varepsilon^2 f_i^{(2)} + \vartheta(\varepsilon^3) \\ \partial_t &= \varepsilon \partial_{t1} + \varepsilon^2 \partial_{t2} + \vartheta(\varepsilon^3) \\ \vec{\nabla} &= \varepsilon \vec{\nabla}^{(1)} + \vartheta(\varepsilon^2) \end{aligned} \tag{2.40}$$

The different magnitude components of the distribution functions and gradients are scaled by their order in the Knudsen number so that they can all be treated at the same level. Therefore, these expansions are inserted into the Taylor expansion of the standard Boltzmann evolution equation and the terms of the same order in ε are balanced. It is assumed that the collision operator does not have a constant contribution for the $\vartheta(1)$ term because it depends on the gradients of the densities; therefore, the equilibrium distribution given in Equation 2.14 is used for the first order term of the distribution function expansion, which allows the macroscopic differential equations to be expressed in terms of the lattice Boltzmann variables [36]. Shan and Doolen (1995) performed this analysis on the Shan-Chen multicomponent model and were able to group the lattice Boltzmann dynamics terms to recover the macroscopic continuity and Navier-Stokes equations:

$$\frac{\partial \rho}{\partial t} + \nabla \cdot (\rho \vec{\mathrm{u}}) = 0 \tag{2.41}$$

$$\rho \left[\frac{\partial \vec{\mathrm{u}}}{\partial t} + (\vec{\mathrm{u}} \cdot \nabla)\vec{\mathrm{u}} \right] = -\nabla \rho + \nabla \cdot [\rho \nu (\nabla \vec{\mathrm{u}} + \nabla \vec{\mathrm{u}}^T)] + \rho \vec{\mathrm{g}}$$

where p is the fluid pressure, ν is the kinematic viscosity, and $\rho\vec{\mathrm{u}}$ is defined as the total momentum and ρ is the total density for both fluids combined. In terms of the lattice Boltzmann parameters these values were identified as:

$$\nu_\sigma = c_s^2 \left(\frac{1}{\omega_\sigma} - \frac{1}{2} \right)$$

$$p = c_s^2 \left[\sum_\sigma \rho_\sigma + \sum_{\sigma\bar{\sigma}} G_{\sigma\bar{\sigma}} \rho_\sigma \rho_{\bar{\sigma}} \right] \tag{2.42}$$

$$\rho \vec{\mathrm{u}} = \sum_\sigma \sum_i f_i^\sigma c_i + \frac{1}{2} \sum_\sigma \vec{\mathrm{F}}_\sigma$$

$$\rho = \sum_\sigma \rho_\sigma$$

Thus the Chapman-Enskog expansion completes the description of the relevant macroscopic variables in terms of the distribution functions.

3. Droplet Formation in Microfluidic Cross-Junctions

3.1 Dimensionless Formulation

Dimensionless formulations provide an appropriate place to start for any fluid dynamics discussion. An analysis of the relative forces occurring for a particular physical phenomena not only helps reduce the number of variables required to describe the system, but also helps pinpoint the driving factors that need to be controlled to produce a desired result. For most microfluidic systems, the small confined length scales exacerbate the effects from viscous and interfacial forces; therefore, a different set of dimensionless numbers are used to describe the dynamics compared to typical macroscopic flows. For example, consider the Reynolds number:

$$Re = \frac{\rho \vec{u}_c l_c}{\mu} \tag{3.1}$$

where μ is the dynamic viscosity, $\vec{u}_c$ is a characteristic velocity and l_c is a characteristic length both of which are specified by convention for a particular system. The Reynolds number is typically employed to distinguish different macroscopic flow regimes; however, the small velocities and length scales in microchannels typically limit the fluid to Stoke's flow. This suggests that the magnitude of the viscous forces greatly exceed the magnitude of the inertial forces. Similarly, the Bond number is generally small as the interfacial forces trump gravity. Because these values have such small magnitudes, they generally provide negligible contributions to microfluidic phenomena [16, 37]. Therefore, the Capillary number is

often a suitable dimensionless number to characterize microfluidic flows because it represents the relative magnitudes of the dominant viscous and surface tension effects. The Capillary number is defined as:

$$Ca = \frac{\mu \vec{u}_c}{\gamma} \tag{3.2}$$

where γ is the fluid-fluid interfacial tension. Another relevant dimensionless quantity sometimes used to characterize microfluidic flows is the Weber number:

$$We = \frac{\rho \vec{u}_c{}^2 l_c}{\gamma} \tag{3.3}$$

which is a measure of the relative contributions from inertial and interfacial effects. However, it should be noted that the Weber number becomes important for relatively larger flow velocities because of the second order dependence. Additional relevant dimensionless groupings become apparent from the dimensional analysis of a specific microfluidic system.

Droplet generation represents the most fundamental functionality for all segmented flow microfluidic applications; therefore, this paper focuses on the hydrodynamics of one of the more simple yet versatile methods – the cross junction. It has been demonstrated that the cross-junction geometry can be used over a range of viscosities and surface tensions and with different flow configurations [4, 13, 38, 39]. Although this geometry is versatile, as with most other microfluidic devices, there are numerous parameters that need to be considered. For the basic cross-junction design with two lateral continuous phase inlets, a main dispersed phase inlet, and a common outlet (See Figure 2), eleven measurable parameters were identified that affect the resulting droplet length: the widths of the lateral and main inlets (w_c and w_d), the lateral and main channel average inlet velocity magnitudes (v_c and v_d), the viscosities of the continuous and dispersed phases (μ_c and μ_c), the densities for both phases

(ρ_c and ρ_d), and the liquid-liquid, continuous phase-solid, and dispersed phase-solid interfacial tensions ($\gamma_{c,d}$, $\gamma_{c,s}$, $\gamma_{d,s}$). Application of Buckingham's Pi Theorem suggests that the droplet size calculation can be reduced from eleven measured parameters to eight dimensionless variables because there are three fundamental dimensions (mass, length, time) [40]. Therefore, the dimensionless expression for droplet-formation takes the form:

$$\hat{d} = \frac{l_{drop}}{w_d} = f(Re, Ca, We, \cos\theta\,, \breve{w}, \breve{v}, \breve{\mu}, \breve{\rho}) \tag{3.4}$$

where d is the dimensionless droplet length, θ is the contact angle for the droplet phase , $\breve{w}$ is the dimensionless channel width ratio, $\breve{v}$ is the ratio of the average inlet velocities, $\breve{\mu}$ is the ratio of the continuous and dispersed phase viscosities, and $\breve{\rho}$ is the ratio of the densities. The additional dimensionless variables used the following conventions:

$$\begin{aligned} \cos\theta &= \frac{\gamma_{c,s} - \gamma_{d,s}}{\gamma_{c,d}} \\ \breve{w} &= \frac{w_d}{w_c} \\ \breve{v} &= \frac{v_d}{v_c} \\ \breve{\mu} &= \frac{\mu_d}{\mu_c} \\ \breve{\rho} &= \frac{\rho_d}{\rho_c} \end{aligned} \tag{3.5}$$

In accordance with the literature, some of these parameters have larger effects on the droplets size compared to others. For example, the Reynolds and Weber numbers were determined to be sufficiently small where their effects were considered negligible [16,41]. In addition, the density ratio is usually very close to unity and would not experience large fluctuations in magnitude for the different chemical

systems. Therefore, this paper will mainly focus on the effects of the capillary number, the contact angle, channel width ratio, the inlet flow velocity ratio, and the viscosity ratio.

3.2 Empirical Investigations of the Cross-Junction Dimensionless Parameters

Several authors have investigated the effects of the capillary number on the cross-junction and flow-focusing geometries. It should be noted that the cross-junction and flow-focusing geometries generate drops using the same mechanisms; in the four-way junctions, the viscous stresses of the encroaching continuous phase compete with the capillary pressure at the interface of the dispersed phase, which are the forces that are compared by the Capillary number [42]. However, the flow-focusing geometry is distinguished from the base cross junction because the outlet has a constricting orifice. Generally, the capillary number is defined using the inlet velocity and viscosity of the more viscous phase with the interfacial tension between the two fluid phases [42]. At low Capillary numbers ($Ca << 1$), the interfacial tension dominates, and therefore the droplet sizes depend more on the geometry of the device [41]. On the other hand, at high Capillary numbers ($Ca >> 1$), viscous effects dominate leading to different droplet deformation regimes [42]. These relations have been observed experimentally for both the cross-junction and flow-focusing geometries. Tan et al. (2008) demonstrated a decrease in droplet size with increasing Capillary numbers in the cross-junction configuration [38]. For the flow-focusing geometry, Lee et al. 2009 demonstrated how the Capillary number could be used to distinguish the different droplet generation regimes. Going from low to higher Capillary numbers they observed transitions from squeezing to threading to dripping regimes for nearly all the viscosity ratios [41].

There have several papers that experimented with different surface tensions and wetting conditions for the segmented microfluidic flows [43,44,45]. The three general wetting scenarios in the literature involve microfluidic devices where: the dispersed phase is wetting while the continuous phase is non-wetting, the dispersed phase is non-wetting while continuous phase is wetting, or the both phases partially wet. For example, Nisisako et al. (2002) demonstrated how it is impossible to create encapsulated droplets in a microchannel when the dispersed phase wets the wall [43]. When the continuous phase preferentially wets over the dispersed phase, droplets can be generated that retain a thin layer of the continuous phase that separate the droplets from the wall [44]. These encapsulated droplets that nearly fill the channel were coined "plugs." Finally, when both fluids partially wet the microchannel walls, Dreyfus (2003) reported erratic droplet formations where the droplets were able to adhere to the channel walls [45].

In terms of the geometrical configurations, we are unaware of any present paper that investigated the effect of the channel width ratio for the cross-junction. However, Lee et al. 2009 conducted a thorough investigation of the flow-focusing design geometries [41]. The asymmetry of the flow-focusing design introduces more geometrical parameters; however, the authors chose to focus on the expansion ratio, which was defined as the ratio between the outlet channel diameter and the orifice diameter. They found that smaller expansion diameters led to higher maximum velocities at the center of the outlet channel, which had a significant impact on the threading droplet formation regime. The larger velocities extended the thread lengths further through the orifices, resulting in smaller droplets [41].

One of the most easily controlled parameters for droplet generation in the cross-junction and flow-focusing designs is the flow rate ratio; therefore, there are numerous papers that have explored this effect. Tan et al. (2008) achieved smaller plug sizes with smaller flow velocity ratios (larger

continuous phase velocities compare to the dispersed phase velocities) for the cross-junction geometry [38]. When the flow ratio was small with large capillary numbers, a streaming regime was observed where plugs no longer formed; instead, a laminar stream of the dispersed phase traveled down the outlet channel sandwiched between the two continuous phases in contact with the channel walls. For the flow-focusing design, Anna et al. (2003) and Lee et al. (2009) also reported that the droplet diameter generally decreased with decreasing inlet velocity ratios [41, 46]. Nie et al. (2008) reported the same trend for a range of viscosity ratios [47].

Lastly, several papers have also demonstrated the impact of the viscosity ratio on the droplet formation mechanism and resulting size. For example, Tan et al. (2008) found that increasing the viscosity of the continuous phase (or decreasing the viscosity ratio) led to slightly smaller droplet sizes [38]. For the flow-focusing design, Nie et al. (2008) found that the viscosity of the dispersed phase had a larger impact on the droplet size [47]. While they did not observe any uniform impact of the viscosity ratio on droplet size, they did notice that the higher viscosities for the dispersed phase were less sensitive to changes in the inlet velocity ratio.

3.3 LBM Investigations of the Dimensionless Parameters in Microfluidic simulations

There have been several recent papers that have employed the Lattice Boltzmann Method to investigate droplet formation at microfluidic junctions [16, 39, 48, 49]. However, these methods have typically employed the color gradient or free-energy LBM schemes in an attempt to reduce the spurious velocities at the interface. While these methods were successful in reducing the size of the spurious currents, they reduced the local nature of the simulation and created additional computational cost. In

addition, none of the papers addressed the impacts of the wetting regimes and device geometry on the droplet formation.

Dupin et al. (2006) investigated several parameters of the flow-focusing design using a variation of a color-gradient flavor of LBM [49]. This method is generally based on calculating the direction of the color-gradient (each phase is represented by a different color) and maximizing the flux of particle distributions against this diffusional gradient. While the method resulted in the desired reduction of spurious velocities and their results matched well with the findings of Anna (2003), their paper expressed little discussion about the flow conditions required to achieve the different droplet sizes and formation regimes. In addition, the paper only conducted simulations using a preferential wetting condition for the continuous phase [49].

Wu et al (2008) employed a variation of the color-gradient method to simulate droplet formation in the cross-junction design in both 2D and 3D [39, 48]. Similarly to Dupin et al.'s (2006) work, Wu et al. (2008) was able to reduce the spurious currents and adopted the same wetting convention. From their simulations, they were able to identify three stages of droplet formation: expansion, necking, and figuration. Similar to the literature reviewed above, they observed smaller drops at higher frequencies with larger capillary number flow. It should be noted that they used the viscosity and inlet velocity of the dispersed phase for their Capillary number calculations. In addition, they investigated the effect of the Weber number. As expected, the Weber number had less of an impact on droplet formation at low inlet velocities; however, its effects became measurable for higher flows [39].

Most recently, Liu and Zhang (2011) used a free-energy model to simulate droplet formation at a cross-junction [16]. Instead of the color-gradient approach, they used a variation of the Ginzburg-Landau free energy method initially developed by Swift (1996) in which phase separation is induced

according to natural thermodynamic parameters. Similar to the papers described above, they were able to reduce spurious velocities at the interface and employed the continuous phase wetting convention. In their paper, they focused on the dimensionless capillary number, inlet velocity ratio, and viscosity ratio. In their analysis of the effects of the capillary number, they observed trends similar to Tan et al (2008)'s findings of smaller droplets from higher capillary flows. It should be noted that these authors used the viscosity and inlet velocity of the continuous phase for their Capillary number calculations instead of the dispersed phased convention used by Wu et al. (2008). For the flow-rate ratio, they also made observations consistent with the literature; however, they identified a critical capillary number at which the droplet diameter no longer follows a power-law relation and the effect of the flow rate ratio weakens. Above a capillary number of 0.024, the droplet diameter was independent of the flow rate ratio. Finally, for the viscosity ratio, they observed a weak dependence of the droplet diameter similar to the findings from Tan et al. (2008). The droplets became slightly smaller for increased viscosity ratios [16].

In this present study, the multicomponent multiphase Shan-Chen Lattice Boltzmann model was used to investigate the factors that controlled the size of the droplets generated by the cross-junction. Each of the parameters identified through the above dimensional analysis will be addressed, and the results will be compared to the empirical and numerical findings from the literature. Because the forces simulated by the Shan-Chen interaction parameter and the bounce back wall densities have a large impact on the surface tensions, the fluid immiscibility, and the range of flow velocities that provide numerically stable results, the proper choice of these parameters was first verified by contact angle measurements. For the cross-junction experiments, the boundary conditions prevented direct control of the inlet velocities; therefore, various Capillary number and flow ratios were tested for fixed contact

angles, viscosity ratios, and channel width ratios. The droplet sizes were measured for conditions that produced stable droplet generation and compared using contour plots.

4. Results and Discussion

All of the simulations discussed below were coded in C++ using the Palabos open source libraries (http://www.palabos.org/). Data visualization and multiphase interface measurements were achieved using Paraview open source scientific visualization software (http://www.paraview.org/).

4.1 Contact Angle Measurement

In order to investigate the effects of surface tension on the cross-junction droplet formation, the lattice Boltzmann interaction parameters needed to be correlated to the macroscopic contact angle. Huang et al. (2007) proposed a version of Young's contact angle relation in terms of the Shan-Chen force terms:

$$\cos\theta = \frac{G_{ads,c} - G_{ads,d}}{G\left(\frac{\rho_d - \rho_c}{2}\right)} \tag{4.1}$$

where the $G_{ads,d}$ is the wall adhesion parameters for the dispersed phase, $G_{ads,c}$ is the wall interaction parameter for the continuous phase, G is the fluid-fluid interaction parameter, ρ_d is the density of the dispersed phase, and ρ_c is the density of the continuous phase dissolved within the droplet phase [50].

Because the present study employed a bounce-back wall density method instead of independent wall interaction parameters, Equation 4.1 was modified slightly to demonstrate that the contact angle no longer depended on the interaction parameter G:

$$\cos\theta = \frac{2(\rho_{wall,d} - \rho_{wall,c})}{\rho_d - \rho_c} = \frac{2\,\Delta\rho_{wall}}{\rho_d - \rho_c} \tag{4.2}$$

where $\rho_{wall,d}$ and $\rho_{wall,c}$ are the artificial bounce-back densities imposed for the dispersed and continuous fluid lattices. Comparing Equations 4.1 and 4.2, it should be noted that the dispersed and continuous phase wall densities are reversed in the numerator because the dispersed phase wall interaction term depends on the continuous phase bounce back wall density.

The contact angle predictions were verified with numerical simulations using the same method described by Huang et al (2007) [50]. A 200x100 size lattice was created with bounce-back boundaries at the top and bottom lattice edges and periodic boundaries at the left and right edges. Periodic boundaries simply transfer the distribution functions that leave from the left lattice edge to the right lattice edge (and vice versa) to create an effectively continuous domain. An initial rectangular shaped droplet of size 40x20 l.u. was placed in contact with lower bounce back surface at the mid-point, and the dimensions of the resulting droplet were measured after 24,000 iterations. The measurements followed the method outlined by Huang et al. 2007 in which the base and height of the droplets are used to calculate the contact angles according to Equations 4.3 [50]:

$$R = \frac{4H^2 + B^2}{8H} \tag{4.3}$$

$$\theta = \frac{B}{2(R - H)}$$

where R is the radius of the droplet, θ is the contact angle, H is the height of the droplet away from the bounce back wall at the droplet midpoint, and B is the width of the droplet base in contact with the wall.

The contact angle was varied by changing the effective densities for the bounce-back walls according to Equation 4.2.

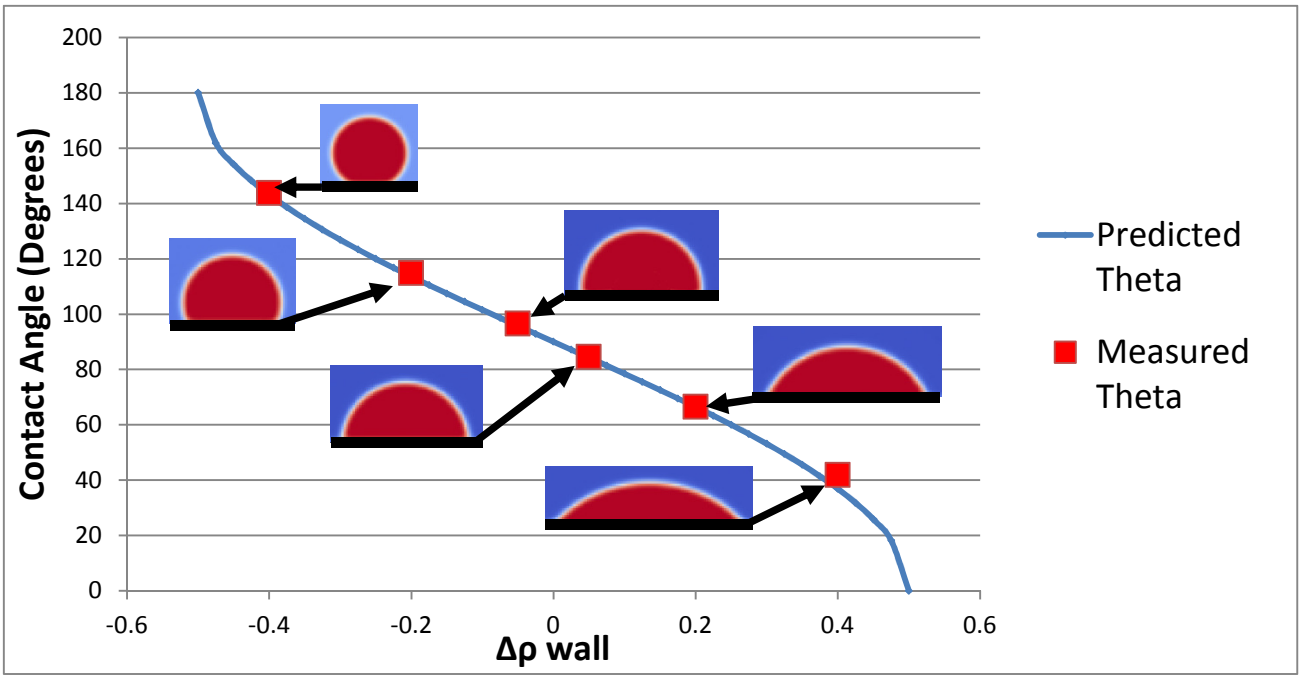

Figure 7. The contact angles predicted using Equation 4.2 and the contact angles measured though 24000 TS of a Shan-Chen LBM simulation were in agreement; thus, the Shan-Chen model provided sufficient control for this dimensionless parameter. The contact angle was specified a priori through the manipulation of the bounce-back wall densities independent of the interaction parameter.

Figure 7 demonstrates how the contact angle measurements were in excellent agreement with the values predicted from just the imposed bounce-back wall densities. The contact angles depicted in Figure 7 were representative of those used in the cross-junction experiments. The most challenging part of the of the contact angle measurements was determining the droplet's base and height, which most likely introduced the largest source of error. Huang et al. (2007) defined the interface location as the position where the dispersed droplet density reached half of the bulk droplet density [50]. In a similar fashion, the interface was defined by averaging the points closest to the transition region that had a density within 90% of the maximum and 110% of the minimum densities along the base and height

vectors. The contact angle was found to be independent of the value of the Shan-Chen interaction parameter G (G =1.3 and G=2 used) as long as the requirement, $1.6 < G\rho_T < 2.0$, prescribed by Huang et al. (2007), was fulfilled where ρ_T is the total sum of both fluid densities at each node [50]. The values for ρ_T, and thus the value of $(\rho_d - \rho_c)$ used in the contact angle measurements, were controlled by choosing appropriate initialization densities for the droplet and the continuous fluids.

4.2 Cross-Junction Simulations

4.2.1 Limits of the Shan-Chen model

The use of a force term to implement the immiscible fluid repulsion places a constraint on the velocities used for the immiscible flow simulations. The immiscible fluid repulsion and solid surface interactions are implemented using a force term that is added to the equilibrium velocity (see Equations 2.34, 2.37, and 2.39); therefore, the combined effects from the forces and fluid velocities need to be below a critical value in order for the low Mach number assumption to hold. When this assumption is violated, the simulation becomes unstable and the velocities can exponentiate towards positive and negative infinity. This makes the choice of a proper interaction parameter, G, extremely important as it determines the magnitude of all the Shan-Chen fluid forces. In order to promote a wider range of feasible fluid velocities, one would choose a value of G as low as possible. However, there is a critical value of G required for phase separation to occur. Increasing the value of G beyond this critical value increases the effective fluid immiscibility and decreases the width of the fluid-fluid interface. Sukop and Thorne (2006) and Huang et al. (2007) reported that a good compromise between these opposing requirements is when $1.6 < G\rho_T < 2.2$ [22, 50]. This suggestion and some additional trial and error

yielded G = 1.3 as a suitable interaction parameter that maintained immiscibility for the range of the density and velocity fluctuations during the cross-junction droplet formations.

Another limitation of the Shan-Chen model was the choice of suitable boundary conditions for immiscible fluid injection. Proper constant velocity conditions have yet to be identified for the Shan-Chen model since both lattices require some density at each boundary and the effects of the lattice interaction needs to be accounted for in terms of the velocity correction [51]. To further elucidate the problem, consider the case of the cross-junction where one wishes to inject only the dispersed phase at the main inlet. Both lattices exist across the entire simulation domain, but the repulsion force is not strong enough to completely eliminate all of the continuous phase particle populations from the regions with high dispersed phase densities – similar to natural diffusion, there is a huge entropic energy cost to maintain a perfectly pure phase, and as result, there is always some amount of continuous phase particle densities throughout the lattice. This means that one cannot arbitrarily set the continuous phase density to zero at the dispersed phase injection site. Even if the continuous phase is set to a negligible density, this establishes a density/pressure gradient for the continuous phase that opposes the desired flow direction for the dispersed phase. In addition, one cannot set the velocity of the continuous phase to zero at the boundary since the zero velocity condition is disrupted by the velocity correction from the interaction potential.

A suitable boundary condition for the injection of a single fluid in multicomponent fluid flow was proposed by Latt et al. (2004) in which they created a “semi-permeable” membrane for selective flow of a desired phase [52]. The semi-permeable membrane was created by imposing a bounce-back boundary for one lattice phase with a Zou-He constant density boundary for the injected phase. For the injection of dispersed phase, a bounce-back boundary across the main inlet on the continuous phase lattice induces a zero velocity condition and prevents any outflow of particle densities. In order for the

dispersed phase to penetrate into the channel that is initially occupied by the continuous phase, Sukop and Thorne (2006) and Latt (2004) suggested the inclusion of a body force to help exclude the continuous phase, which was considered analogous to a pressure gradient [22, 52]. In addition to the inlet body force, the imposed $\rho_{wall,c}$ bounce back density at the semi-permeable boundary provides some control of the lattice interaction at the interface, which can be used to manipulate the boundary velocity for the dispersed phase. As a result, the constant-density, semi-permeable boundary conditions made it difficult to control the Capillary numbers for the injection of each respective phase especially since the resulting inlet velocities were affected by the interaction of the impinging flows. Because the outlet density experiences large fluctuations depending on which phase is exiting, a Zou-He constant velocity boundary condition was applied for the outlet. Therefore, with the stability restrictions imposed by both the interaction parameter and the boundary conditions, the flow conditions used in the analysis of the cross-junction droplet formation were the result of trial and error for stable flow conditions. A systematic analysis of the boundary condition parameters and the resulting flow conditions will be addressed in future studies.

Finally, one of the most glaring inaccuracies of the Shan-Chen model is the presence of spurious velocities at the fluid interfaces. Shan (2006) suggested that the artificial velocities are a result of the lack of isotropy of the D2Q9 lattice with the curved fluid interfaces – the insufficient symmetry of the repulsive force terms are not completely balanced, which results in residual velocities [53]. Figure 8 demonstrates a typical velocity field immediately after droplet generation. The magnitudes of the spurious velocities greatly exceed the magnitudes of the minute capillary flows. Such large spurious velocities limit the cross junction to small Capillary and Weber numbers. Nonetheless, the plug-like flow-field in the dispersed and continuous phases is in agreement with the velocity field reported by Wu et al. 2008 even when the spurious currents were reduced by using a color-gradient based method [39].

Furthermore, Wu et al. (2008) verified the plug-like flow-fields with micro-PIV measurements of a fabricated cross-junction. However, it should be pointed out that the plug-like flow contradicts the

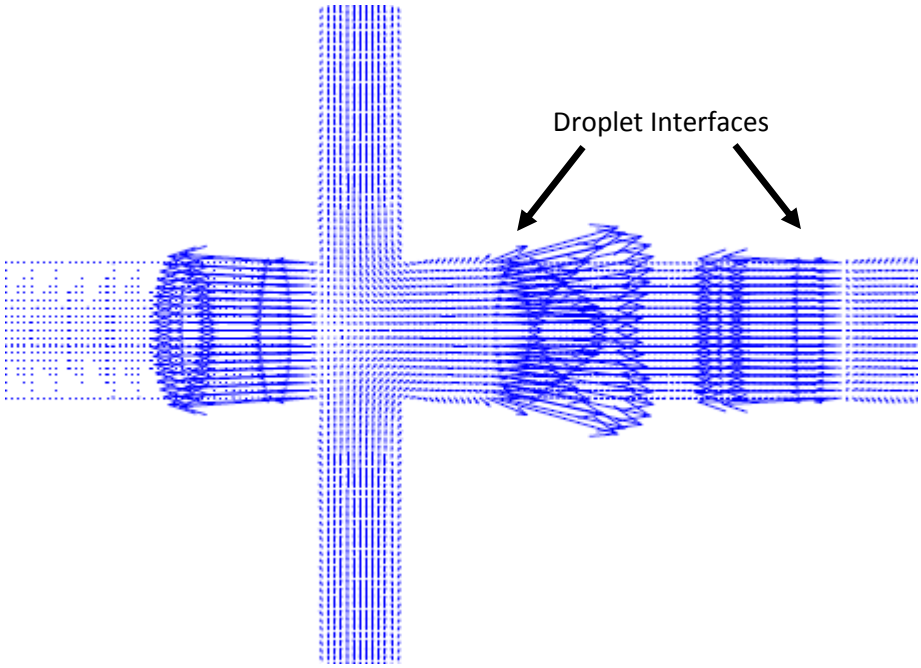

Figure 8. A typical velocity field observed after the generation of a droplet. The artificial large vectors at the fluid interfaces are the spurious velocities that result from the lack of isotropy from the repulsive force terms in the Shan-Chen model.

studies that suggest the presence of diametric vortices within the droplet that are believed to promote mixing as it traverse the capillary channel [7,54]. This could be due to the lack of the thin lubrication layer of the continuous phase between the droplet and the capillary wall in the cross-junction trials reported in this paper.

4.2.2 Cross-Junction Flow Regimes

Within the flow-velocity limitations of the Shan-Chen model, there were distinct flow patterns identified throughout all the cross-junction trials: retraction, streaming, threading, and droplet generation. Except for the retraction case, these scenarios have been documented in the literature

[38,39, 41]. The retraction regime describes a scenario where the droplet phase retracts back into main inlet when the impinging lateral channel pressure is too high. Because this scenario is the result of imbalanced constant density boundary conditions and is of little commercial merit, it will not receive any further discussion.

The streaming regime was observed when the Capillary number was sufficiently high and the volumetric flows through the main and lateral channels were nearly balanced. Figure 9 shows the typical flow conditions that resulted in a cross-junction streaming regime. At higher Capillary numbers, viscous forces gain importance and distort the droplet interface. When the volumetric flow rates for both phases, Q_c and Q_d, are balanced, the droplet phase interface is projected down the main channel balanced by the flow of the continuous phase on either side. In two dimensions, the volumetric flow rate ratio can be defined by the velocity ratio and the channel width ratio:

$$\hat{Q} = \frac{Q_d}{Q_c} = \frac{v_d w_d}{2 v_c w_c} = \frac{\hat{v}\hat{w}}{2} \tag{4.4}$$

The factor of 2 in the denominator comes from the fact that there are two lateral channels volumes for the one main channel volume; therefore, streaming was observed when $\widehat{Q}$ neared 0.5.

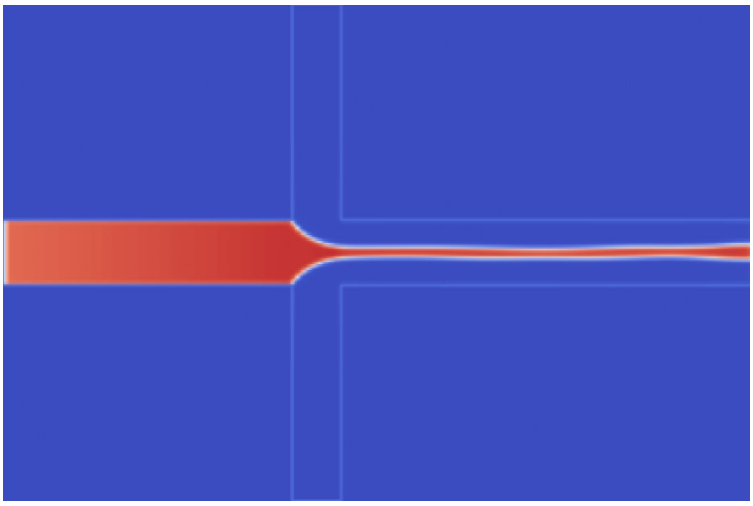

Figure 9. Density field of a typical Shan-Chen LBM simulation resulting in the streaming regime where the inlet volumetric flow rates are nearly balanced. The slight imbalance results in fluctuations in the stream thickness with time. $\hat{v}$ = 0.62, $\hat{w}$ = 1.35 and Ca_c = 8.4e-4. Equation 4.4 gives $\hat{Q} = 0.42$

Another scenario that has commercial merit is the threading regime. Similar to the streaming case, the Capillary numbers that produce threading are sufficiently high to distort the droplet interface; however, droplets pinch off from the thread tip. Figure 10 demonstrates a typical flow condition that induced threading. This regime has the potential benefit of rapid generation of small droplets since the dispersed phase doesn't retract to reform the rounded interface after pinching off a droplet. Lee et al. (2009) focused on characterizing the threading regime in flow focusing devices because it resulted in the

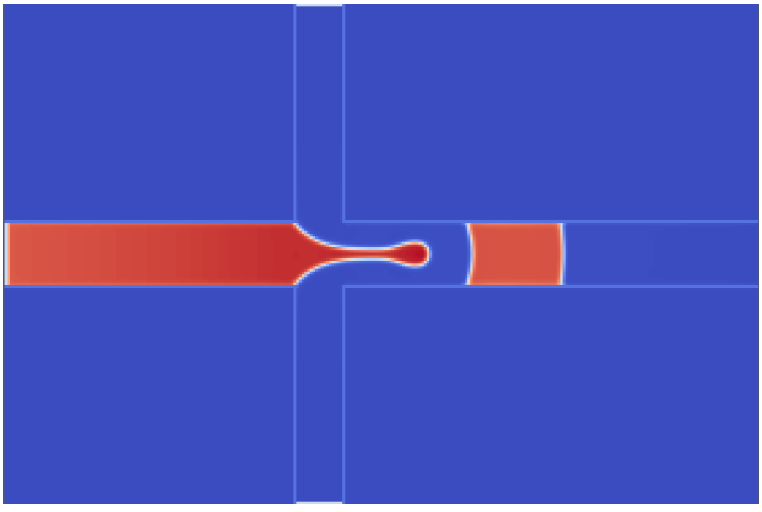

Figure 10. Density field of a typical Shan-Chen LBM simulation resulting in the threading regime. A second droplet is forming at the thread tip almost immediately after the preceding droplet. Threading typically occurred at larger Capillary numbers with $\hat{v} \approx 1$. In this simulation, Ca_C = 8.0e-4, $\hat{v}$ = .997, $\cos\theta$ = .1, and $\hat{\mu}$ =.54

rapid generation of the smallest precise droplets [41]. Similar to the findings in this paper, there was a critical capillary number for the threading regime with smaller droplets produced at higher capillary numbers. However, the threading scenario required extremely precise control of the flow velocities in order to generate droplets with precise volumes. Threading that resulted in uniform droplet generation was observed in the cross-junction configuration when $\hat{v}$ was very close to unity, and because the flow velocities were very difficult to control in the simulations described in this paper, the threading regime almost always resulted in non-uniform droplet generation.

The typical droplet generation regime that was the focus of this study is depicted in Figure 11. In accordance with empirical findings and the LBM simulations of Wu et al (2008) and Liu and Zhang (2011), the three distinct phases of the uniform droplet generation regime was observed: expansion, necking, and figuration [16, 39].

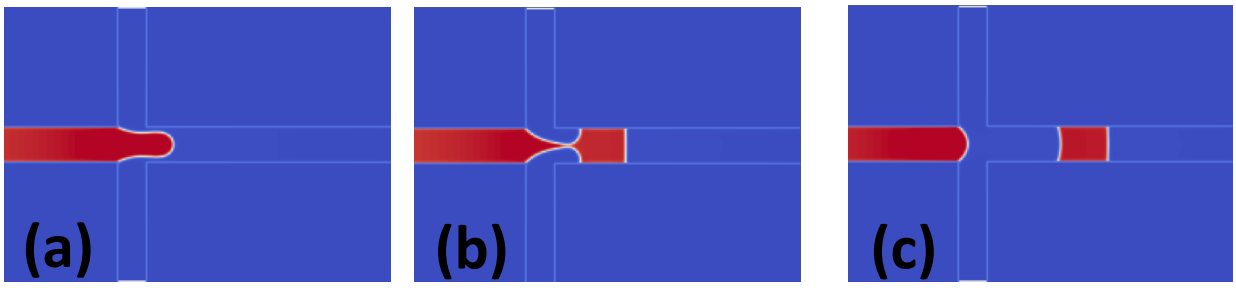

Figure 11. The three main stages of the uniform droplet generation regime. (a) Expansion of the droplet into the channel builds up the pressure in the lateral channel. (b) the accumulated lateral channel pressure differential overcomes the droplet surface tension creating a neck within the dispersed phase. (c) the neck collapses with the droplet pinching off and the interfacial tension rapidly regenerates the curved droplet surface

4.2.3 Effect of Capillary Number and Flow Ratio on Droplet Size

Consistent with the literature review, the Capillary number and the flow ratio demonstrated the most significant effects on the size of the droplets generated using the cross-junction configuration. Because the Shan-Chen model provides precise control of the contact angle (verified in Section 3), fluid viscosity (Equation 2.42), and geometry, these parameters were fixed while the inlet bounce-back densities, the inlet body-forces, and the outlet velocity were varied to manipulate the inlet flow rates. It was found that a critical balance between the inlet body-force parameters was required to prevent retraction of the droplet phase; however, it was observed that the body force term had a negligible impact on the Capillary number and flow ratios. The inlet densities for both phases were kept at $\rho = 1$ to reflect the minimal density difference typically observed between to the two phases.

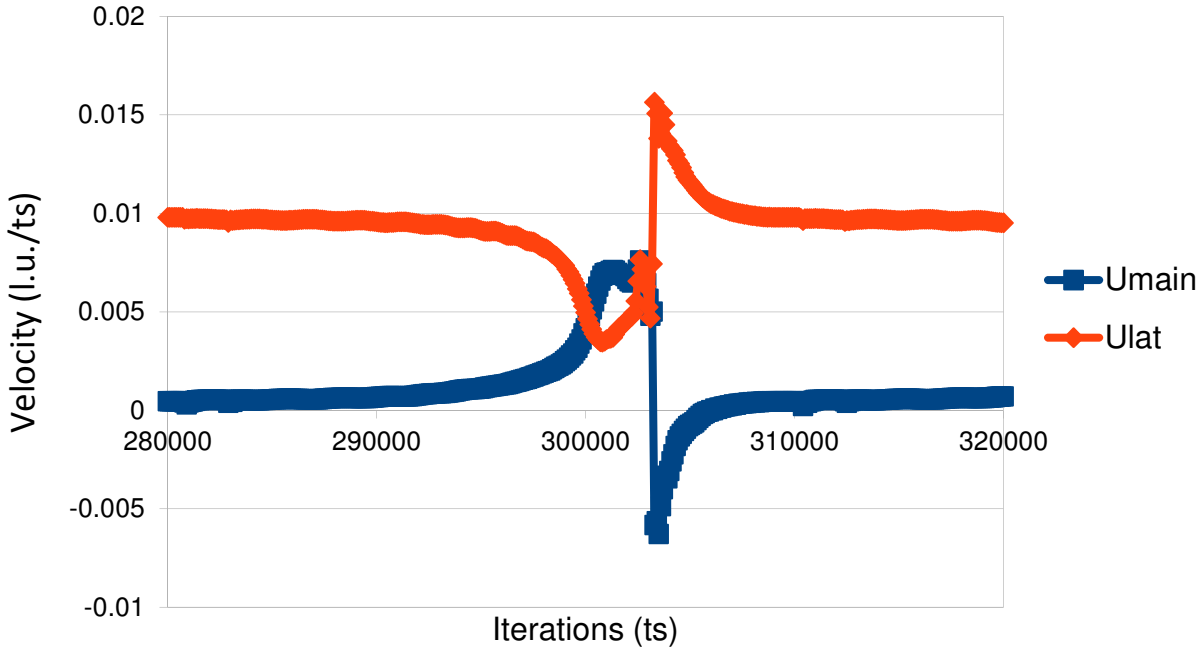

Figure 12. The measured inlet velocities at the lateral and main channels fluctuated over the course of one period of droplet generation. The critical points in the velocity profiles near 300,000 TS represent the transition from the necking to pinch-off phase. The largest magnitude spikes near 303,000 were associated with the retraction of the dispersed phase after pinch-off and the restoration of the continuous phase dominant flow.

The dimensionless numbers were calculated using the average velocities measured at a distance of two channel widths upstream from the junction. The averages were taken over a square box that spanned across the respective dispersed and continuous phase channel inlets. Figure 12 shows the measurements for main channel and lateral channel inlet velocities over the course of one period of droplet generation. The fluctuations in the velocities occur at regular periods that coincide with the different phases of droplet generations. The steady increase in velocity from 280,000 to about 299,000 time steps represents the expansion phase. The growth of the droplet is accompanied with a steady growth of the main inlet velocity coupled with the gradual decline of the lateral channel average velocity due to the droplet obstructing the lateral flow. At about 300,000 TS, necking began resulting in reversing the dip in the lateral velocity and the maximum in the main channel velocity as the clogged lateral flow impinges upon the dispersed phase. At about 302,600 TS, the droplet pinched off, which resulted in a small sharp spike in both velocities. The impinging lateral flow dominated again causing the droplet to retract back into main channel at 303,300 which is accompanied by the large spike into negative velocities. Finally, the main channel rapidly regains velocity as the dispersed phase reenters the junction and the cycle begins again.

As a result of these fluctuations, the calculation of the dimensionless numbers relied on the time averaged values for measured quantities. Comparing the velocity vs. time profiles that resulted in the generation of different sized drops revealed that the smaller drops had smaller spikes in the main inlet velocity with respect to both magnitude and duration; therefore, these fluctuations needed to be included in the measurement averages in order to observe the effects of the flow velocities. Thus, the reported Capillary numbers and flow ratios reflect the average velocities across the channel widths and the time average over one period of droplet generation. In addition, this method is in agreement with

the empirical measurement methodology as the volumetric flow rates imposed by the pumps during microchannel experiments reflect both a spatial and temporal average velocity.

Figure 13 demonstrates how the capillary number and flow rate ratio determine the size of the droplet. The interpolation method described for the contact angle measurements was also used to determine the location of the droplet interface for the droplet size measurements. The droplet size was determined by measuring the length of the plug at the midpoint of the outlet channel. To analyze the combined effects of the Capillary and velocity ratio on the droplet size, a distance method of interpolation within the Minitab statistical analysis software was used to generate contour plots using a distance power of three. The largest droplets ($\hat{d}$ > 8 in the upper left corner of Figure 13) were produced when the average main inlet velocity was 5 times larger than the lateral inlet velocity and the capillary number of the continuous (carrier) phase was relatively low (Ca_C = 2.7e^{-4}). These conditions allow the dispersed phase to eject more fluid before the lower lateral flow can impinge upon the dispersed phase obstruction. Conversely, larger Capillary numbers for the continuous phase and smaller velocity ratios resulted in smaller droplets ($\hat{d} \sim 1$ in the lower right corner of Figure 13). Larger capillary numbers reflect larger magnitudes of the viscous forces, which facilitate droplet pinch off, and lower flow ratios reflect the greater extent of continuous phase impingement on the droplets. These observations are consistent with the Lee et al (2009), Tan et al (2008), Liu and Zhang (2011) and Wu (2008). In addition, it should be noted that smaller ($\hat{d} \sim 1$) drops were also generated at relatively low capillary numbers if the flow ratio was low enough; however, these droplets had much longer periods of formation. Droplets with lengths less than one main channel width were never observed.

Possible sources of error were identified in the methodology for the droplet size, capillary number, and flow ratio measurements used to construct Figures 13, 14, and 15. To start, the sample population is by no means an exhaustive attempt to quantify the effects of the flow ratio and Capillary

number. With the limited control of the inlet flow rates due to the semi-permeable pressure boundary conditions and the velocity constraints of the Shan-Chen model, the data was clustered near the highest stable capillary numbers and lowest flow ratios (before retraction of the dispersed phase) in an attempt to generate the smallest drops possible. Such small drops would facilitate future studies focusing on droplet mixing for chemical reactions and the subsequent purification of the reaction products. The droplet size measurement was prone to errors associated with the precise identification of the interface locations described in the contact angle measurement section. In addition, the measurements of the average flow velocity and Capillary numbers were prone to errors associated with the sampling method. In an effort to conserve computer memory, measurements were typically taken every 1000 time steps. As a result, some of the rapid fluctuations in velocity were excluded from the time averaging depending on whether the sampling rate was in synch with the droplet generation frequency.

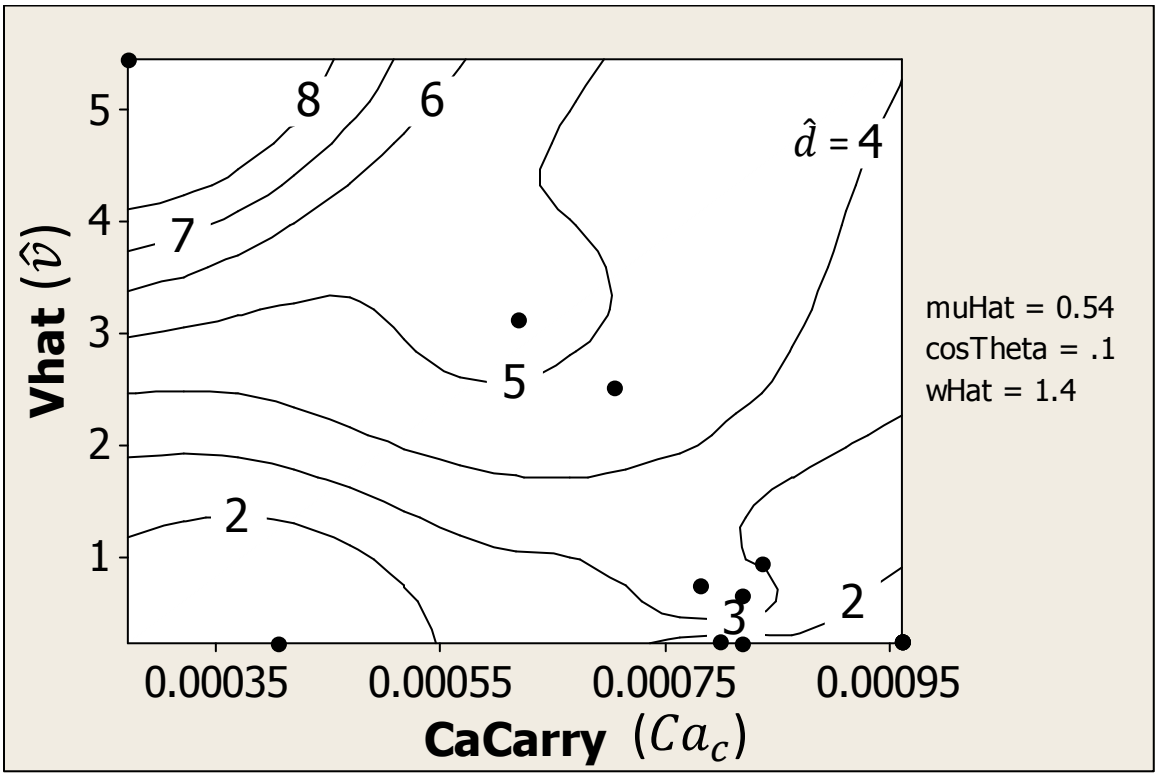

Figure 13. A contour plot demonstrating the combined effects of the flow rate ratio, $\hat{v}$, and the continuous (carrier) phase Capillary number on the lengths of the droplets generated in the cross junction. The ● symbols represent the actual data points used in the interpolation. The smallest drops were generated at higher Ca_c and lower $\hat{v}$.

4.2.4 Effect of Contact angle, Channel width ratio, and Viscosity Ratio

The remaining dimensionless parameters ($\cos\theta$, $\hat{w}$, and $\hat{\mu}$) were observed to have less of an effect on the size of the droplets generated by the cross-junction compared to the Capillary number and flow ratio. Figure 14 shows a comparison of the contour plots for the droplet sizes generated when manipulating the boundary flow conditions for different fixed values of the contact angle, the lateral channel width, and the lattice viscosities.

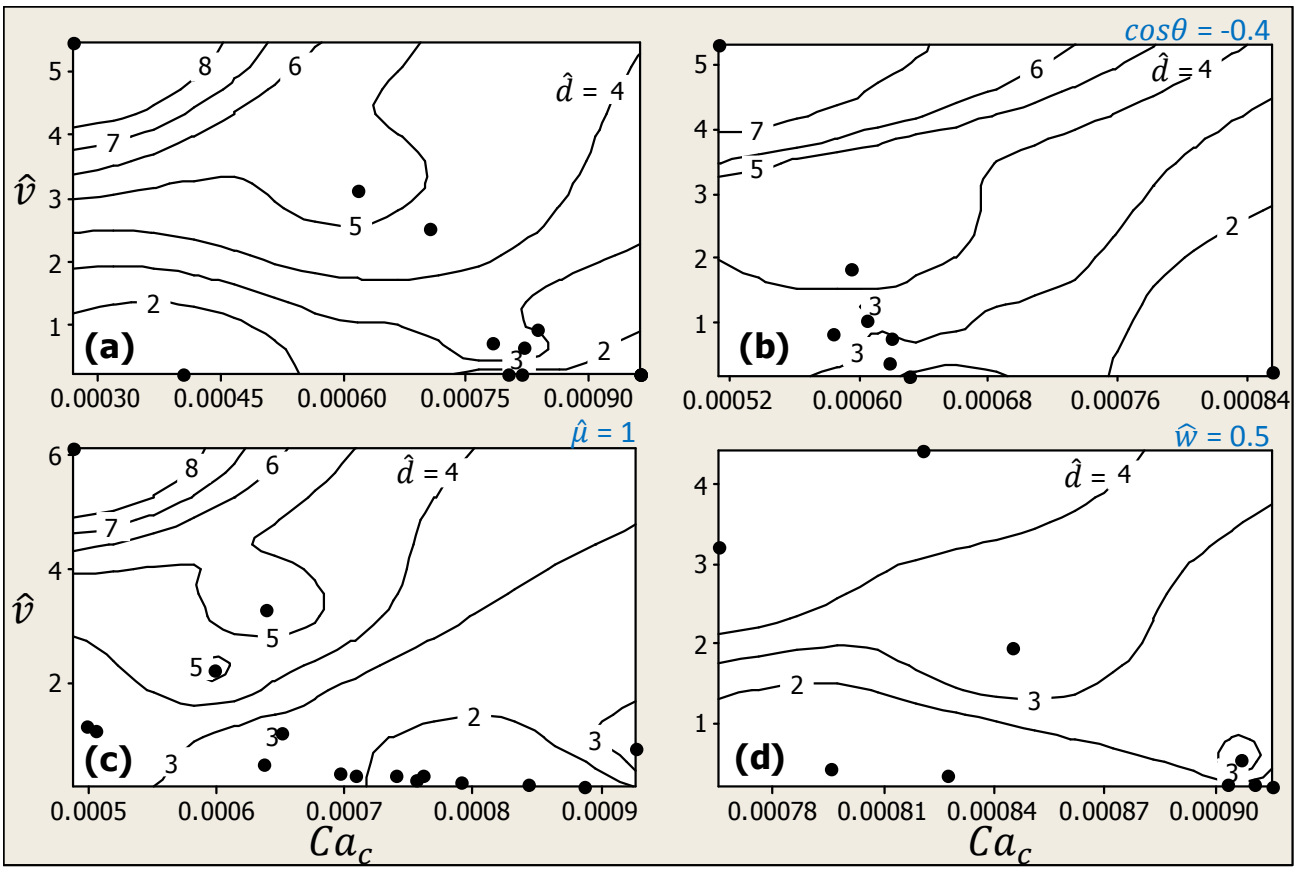

Figure 14. Contour plots generated for various Ca_c and $\hat{v}$ with systematic changes in $\cos\theta$, $\hat{\mu}$ and $\hat{w}$. The ● symbols represent the actual data points used in the interpolation. (a) depicts the droplet size contours for $\cos\theta = 0.1$, $\hat{\mu}$ = 0.54 and $\hat{w}$ = 1.4. (b) demonstrates the effect of the contact angle in comparison to (a) with $\cos\theta = -0.4$, $\hat{\mu}$ = 0.54 and $\hat{w}$ = 1.4. (c) shows the effect of viscosity ratio in comparison to figure (a) with $\cos\theta = 0.1$, $\hat{\mu}$ = 1.0 and $\hat{w}$ = 1.4. (d) provides a comparison for the effects of the channel width ratio with $\cos\theta = 0.1$, $\hat{\mu}$ = 0.54 and $\hat{w}$ = 0.5.

Changing these fixed values typically required a set of optimization experiments to determine a new set of stable boundary conditions within the velocity constraints of the Shan-Chen model. As a result, direct comparison of the same flow conditions for different values of the viscosity ratio, contact angle, and channel width ratio was difficult to achieve. Therefore the effects of these dimensionless parameters were compared using the contour plots generated for the stable range of flow conditions using the two known critical factors (Ca_c and $\hat{v}$) for the graph axes.

Qualitatively, the contour plots all display the same trends for $\hat{v}$ and Ca_c independent of the other dimensionless parameter values: smaller drops were formed at larger Ca_c and lower $\hat{v}$. Because the interpolation method is most accurate within the range of the supplied data and each data-set has a different range of flow condition trials, the contour plots have different axes range. Therefore, Figure 14(a) was chosen as the base contour plot for comparison of the simulations with different $\cos\theta$, $\hat{w}$, and $\hat{\mu}$ values because it represented the largest area in Ca_c , $\hat{v}$ space. Overlaying the points from Figures 14(b), 14(c), and 14(d) on the base plot Figure 14(a) demonstrated that the base contour plot with $\cos\theta$ = 0.1, $\hat{w}$ = 1.4 and $\hat{\mu}$ = 0.54 was sufficient in predicting the droplet sizes when only one of the fixed parameters was changed independently. An example of such an overlay comparison is seen in Figure 15, which compares the droplet size interpolation for two different contact angles.

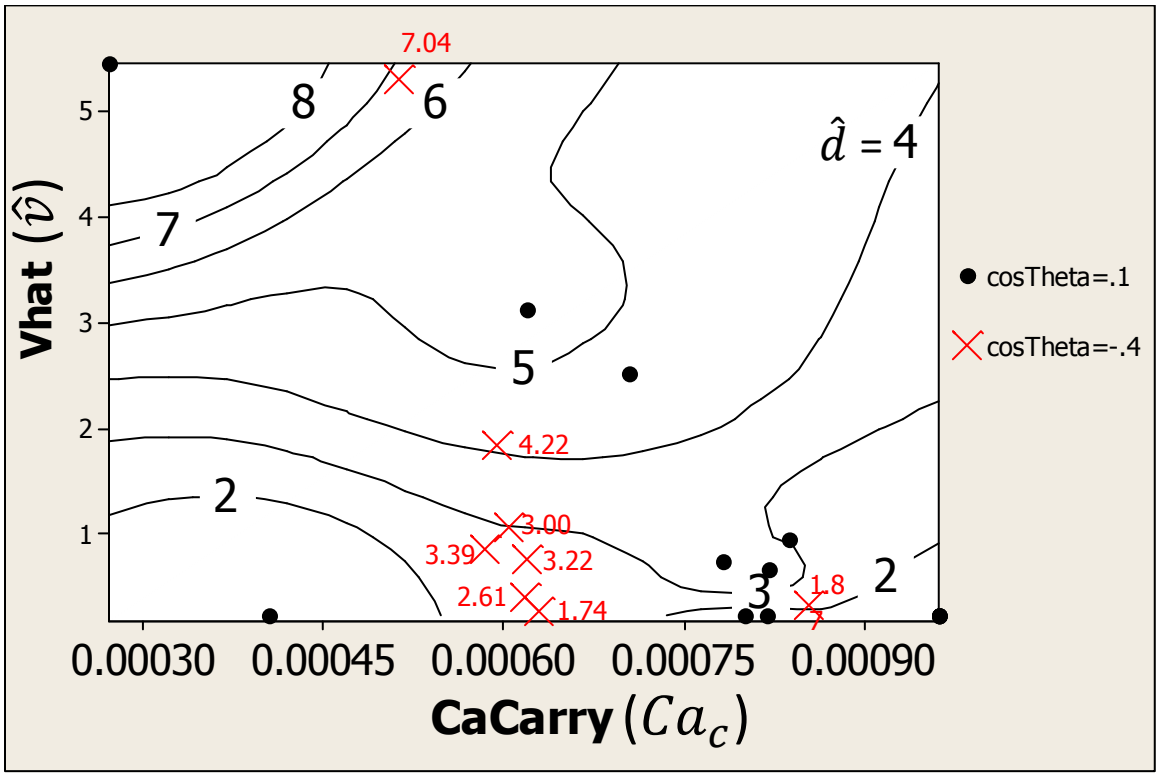

Figure 15. A contour plot with the data from two sets of experiments with different contact angles overlaid. The ● symbols represent the data for $\cos\theta$ = 0.1, and the X symbols represent $\cos\theta$ = -0.4 with the dimensionless droplet sizes posted adjacent to the X symbols. The interpolation for the droplet sizes at various Ca_c and $\hat{v}$ with $\cos\theta$ = 0.1 sufficiently predicts the droplet sizes for simulations with $\cos\theta$ = -0.4 when all the other fixed parameters held constant. The simulations depicted used $\hat{w}$ = 1.4 and $\hat{\mu}$ = 0.54.

The Capillary number and flow rate ratios had the largest impact on the droplet size for the sampled flow conditions, which is in agreement with the findings of Liu Zhang (2011), Lee et al (2009), and Tan et al (2008). Qualitatively, the contact angle, viscosity ratio, and channel width ratio were observed to have an impact on the conditions that define the transitions between the different flow regimes. For example, in the case of the large contact angle ($cos\theta$ = -0.4), threading appeared to occur at wider range of flow conditions, most likely due to the fact that the dispersed phase was less apt to fill the channel width to form a stable plug. The limited sample size and scattered flow conditions attributed to the

limitations of the Shan-Chen model made it difficult to generate a phase diagram that would quantify the shifts in the cross-junction flow regimes.

5. Conclusions and Future Work

In summary, the segmented flow microfluidics could potentially provide a cheaper and more effective alternative to current industrial and laboratory fluid management techniques – the relatively large surface area-to-volume ratios have been demonstrated to provide precise control over reactant volumes, mixing, incubation, and indexing for a wide range of applications. An understanding of the flow conditions required for precise droplet generation is necessary for any segmented flow application and was therefore the focus of this study. The Shan-Chen multicomponent multiphase Lattice Boltzmann method was used to simulate droplet formation conditions because it adequately captures the surface tension effects that are dominant in microfluidic settings. This model provided sufficient control for the contact angles; however, the lack of control of the inlet velocities and the flow restrictions from the large interfacial spurious velocities made it difficult to cover a broad range of flow conditions. Nonetheless, different droplet formation regimes were observed: retraction, streaming, threading, and stable generation. For the range of numerically stable flow conditions tested, the effects of the Capillary number, inlet velocity ratio, contact angle, viscosity ratio, and channel width ratio on the size of the resulting droplets were consistent with the trends described in the literature. The combined effects of the Capillary number and velocity ratio were demonstrated to be the process drivers for the cross-junction droplet size while the other dimensionless numbers had a less significant effect. Qualitatively, the contact angle, viscosity ratio, and channel width ratio were observed to shift the flow conditions for transitions between the stable droplet generation, streaming, and threading regimes;

however, the scattered flow conditions made it difficult to generate a phase diagram for such transitions.

Future work will focus on improving the stability of the model. This will entail the investigation of the color gradient and free energy models described in the literature. The reduced magnitude of spurious velocities will allow a wider range of numerically stable flow conditions, which facilitates the generation of a phase diagram that will characterize the effect of the contact angle, viscosity ratio, and channel width on the transitions between different flow regimes. In addition, rigorous analysis of the constant velocity boundary conditions will be conducted to establish suitable control of the microchannel inlet velocities for the coupled multicomponent model. Furthermore, understanding the mechanism for droplet formation is only a starting point for modeling the segmented flow microfluidic reaction applications published in the literature – see references [7, 13, 55, 56] for examples. Therefore, future studies will involve the inclusion of tracer or suspended particles in order to better quantify the mixing kinetics within the droplets and the flow conditions required for efficient chemical reactions.

Some effort has already been started towards the inclusion of tracer particles into the current Shan-Chen LBM scheme. To start, the combined convection and diffusion of the tracer was verified by simulating Taylor-Aris dispersion for different Péclet numbers. For capillary flow, the dimensionless Péclet number characterizes the ratio between convective and diffusive contributions defined by:

$$Pe = \frac{v_d w_d}{D_t} \tag{5.1}$$

where v_d is the average inlet velocity of the dispersed phase, w_d is the channel width of the dispersed phase, and D_t is the diffusion coefficient of the tracer lattice, which is defined by the same equation for the lattice viscosity in equation 2.42. Taylor (1953) reported the measurements of higher effective diffusion coefficients when a solute was injected into tube with laminar Poiseuille flow [57]; the

effective diffusion coefficient was later named the dispersion coefficient. Based on empirical findings, he was able to derive an expression for the mass flux according to:

$$Q = vC + D^* \frac{\partial C}{\partial x} \tag{5.2}$$

$$\frac{D^*}{D} = 1 + \frac{Pe^2}{210}$$

where Q is the mass flux of solute along the tube axis, C is the average concentration of solute across the tube cross-section, D is the diffusion coefficient of the solute in the solvent, and D* is the dispersion coefficient [22, 58]. In addition to the molecular diffusion in both the radial and axial directions, the solute convects at different rates along the tube axis depending on the radial location due to the parabolic velocity profile. The effective increase in the observed diffusion coefficient, now known as the dispersion coefficient, was attributed to the shear between the velocity lamina. Figure 16 demonstrates how the tracer convection/diffusion scheme adequately captures the Taylor-Aris dispersion; the Péclet numbers tested represent the limits of the range for accurate dispersion measurements ($\sqrt{210}$ < Pe < L/w_d), where L is the length of the channel [22, 58].

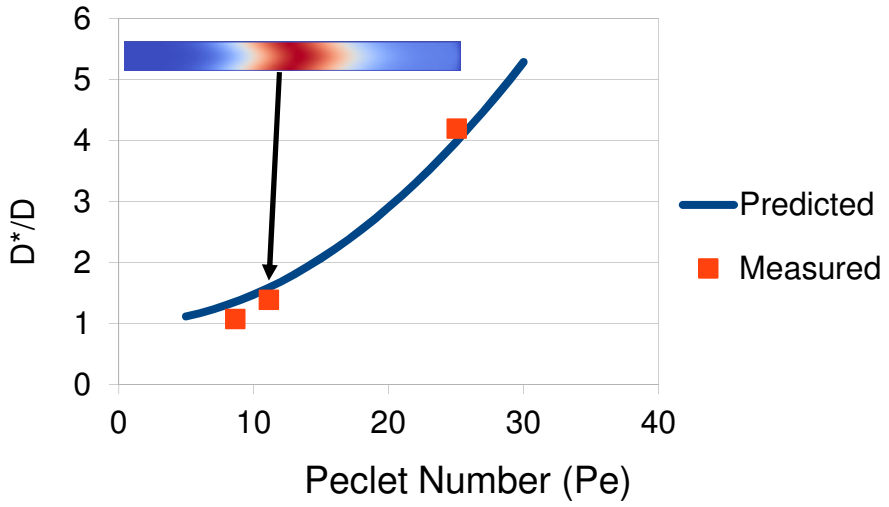

Figure 16. A Comparison of the Taylor-Aris Disperision coefficient measured after 16,000 TS in a 250x23 l.u. slit with Poiseuille flow to the Dispersion Coefficient predicted using equation 5.2. The inset picture on the upper left-hand corner depicts a representative Taylor Dispersion experiment.

Once control over the relative diffusive and convective contributions to the tracer dispersion was established, the tracer model was applied to a configuration consisting of two opposing cross-junctions generating droplets that met head-on at a T-junction. In the Shan-Chen/tracer coupling, the range of stable tracer diffusion coefficients appeared to be linked to the host lattice viscosity, which limited the simulations to relatively low Péclet numbers. As a result, tracer diffusion was significant, and the droplets became fully mixed before reaching the outlet boundary when they met head-on. Interestingly, when the outlet flow velocity was sufficiently low, the resulting back pressure caused interference between the opposing cross-junctions and the droplet generation became out of synch. This phenomenon has been documented in the literature, and provides one of the greatest challenges to scaling the microfluidic platforms for higher throughputs – running multiple devices and functional features in parallel causes a significant degree of interaction amongst the capillary flows [7, 59, 60]. Figure 17 depicts the mixing for the cases where the droplets met head-on at T-junction or when there was a phase lag between the droplet formations.

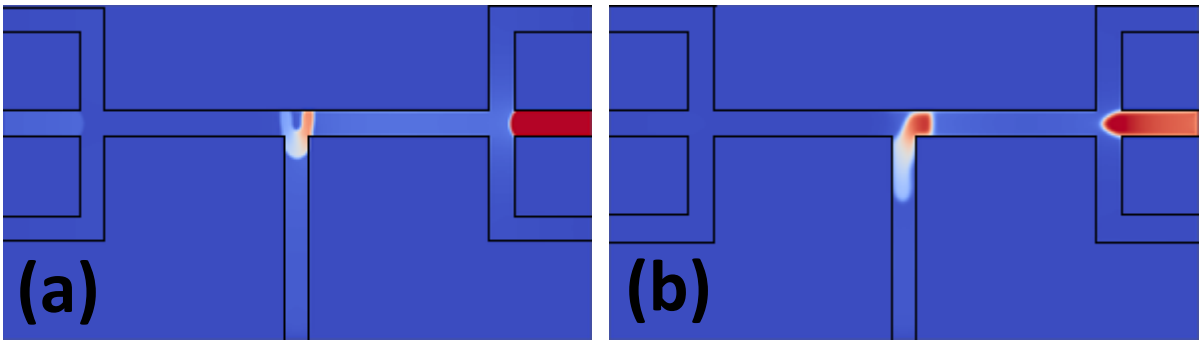

Figure 17. Tracer concentrations Shan-Chen LBM simulations with the inclusion of a tracer lattice that satisfies the advection/diffusion dynamics of Equation 5.2. Two parallel cross-junctions produce droplets that meet at a T-junction (a) Depicts the scenario when the droplets meet head-on, and the mixing upon droplet coalescence at the T-junction is symmetric. (b) Increased back pressure at the outlet causes droplet formation between the two cross-junctions to become out of synch. When the droplets did not meet head-on, the droplet was observed to require longer times for complete mixing.

Therefore, future studies will include further development of the models to quantify droplet mixing. In particular, the goal is to include suspended particles that disperse purely from convective forces. The droplet mixing will then be quantified by measuring the number of time steps required for the spatial concentration distribution to reach an equilibrium value. Such particles can also be used to simulate microfluidic applications that employ functionalized magnetic particles to promote mixing within droplets and capture reaction products.

References

1. B.H. Weigl, R.L. Bardell, and C.R. Cabrera. "Lab-on-a-chip for drug development." *Adv. Drug Del. Rev.*, 2003, 55, p. 349–377.

2. Gijs, M.AM. "Magnetic bead handling on-chip: new opportunities for analytical applications." *Microfluid Nanofluid*, 2004, 1, p. 22–40.

3. Mark, D. et al. "Microfluidic lab-on-a-chip platforms: requirements, characteristics and applications." *Chem. Soc. Rev*., 2010, 39, p. 1153–1182

4. Hung, L.H. "Alternating droplet generation and controlled dynamic droplet fusion in microfluidic device for CdS nanoparticle synthesis." *Lab Chip*, 2006, 6, p. 174–178.

5. Chan, E.M., Alivisatos, A.P., and Mathies, R.A. "High-Temperature Microfluidic Synthesis of CdSe Nanocrystals in Nanoliter Droplets." *J. Am. Chem. Soc*., 2005, 127, p. 13854–13861.

6. Shestopalov, I., Tice, J.D., and Ismagilov, R.F. "Multi-step synthesis of nanoparticles performed on millisecond time scale in a microfluidic droplet-based system." *Lab Chip*, 2004, 4, p. 316–321.

7. Song, H., Chen, D.L., and Ismagilov, R.F. "Reactions in Droplets in Microfluidic Channels." Angew. Chem. Int. Ed. 2006, 45, p. 7336 – 7356.

8. El-Ali, J., Sorger, P.K., and Jensen, K.F. "Cells on Chips." *Nature*, 2006, 442, p. 403–411.

9. Weibel, D.B., and Whitesides, G.M. "Applications of microfluidics in chemical biology." *Curr. Opin. Chem. Biol.*, 2006, 10, p. 584–591.

10. Dittrich, P.S., Tachikawa, K., and Manz, A. "Micro Total Analysis Systems. Latest Advancements and Trends." *Anal. Chem*., 2006, 78, p. 3887–3908.

11. Ahmed, B., Barrow, D., and Wirth, T. "Enhancement of Reaction Rates by Segmented Fluid Flow in Capillary Scale Reactors." *Adv. Synth. Catal*. 2006, 348, p. 1043 – 1048.

12. Song, H. et al. "On-Chip Titration of an Anticoagulant Argatroban and Determination of the Clotting Time within Whole Blood or Plasma Using a Plug-Based Microfluidic System." *Anal. Chem.* 2006, 78, p. 4839-4849.

13. Liau, A. et al. "Mixing Crowded Biological Solutions in Milliseconds." *Anal. Chem*. 2005, 77, p. 7618-7625

14. Hung et al. "Alternating droplet generation and controlled dynamic droplet fusion in microfluidic device for CdS nanoparticle synthesis." Lab Chip, 2006, 6, 174–178

15. Succi, S. “The Lattice Boltzmann Equation: For Fluid Dynamics and Beyond.” Oxford University Press. 2001

16. Zhang, J. “Lattice Boltzmann method for microfluidics: models and applications.” *Microfluid Nanofluid,* 2011, 10, p. 1–28.

17. Hirt, C.W., and Nichols, B.D., “Volume of fluid (VOF) method for the dynamics of free boundary.” *J. Comput. Phys.,* 1981, 39, p. 201-225.

18. Sussman, M., Smereka, P., and Osher, S. “A level set approach for computing solutions to incompressible two-phase flow.” *J. Comput. Phys*., 1994, 114, p. 146–159.

19. Tryggvason, G., Bunner, B., et al. “A front-tracking method for the computations of multiphase flow.” *J. Comput. Phys.,* 2001, 169, p. 708–759.

20. Kadau, K., Germann, T.C., and Lomdahl, P.S. “Molecular-Dynamics Comes of Age: 320 Billion Atom Simulation on BlueGene/L.” *Int. J. Mod. Phys. C,* 2006, 17, p. 1755.

21. Qian, Y.H, D'Humieres, D., and Lallemand, P. “Lattice BGK Models for Navier-Stokes Equation.” *Europhys. Lett.,* 1992, 17, p. 479.

22. Sukop, M.C., and Thorne, D.T. “Lattice Boltzmann Modeling: An Introduction for Geoscientists and Engineers.” Springer 2007.

23. Chapman, S. and Cowling, T.G. “The Mathematical Theory of Non-uniform Gases: An Account of the Kinetic Theory of Viscosity, Thermal Conduction and Diffusion in Gases, Third Edition.” Cambridge Unviersity Press, 1970.

24. Laurendeau, N. M. “Statistical Thermodynamics - Fundamentals and Applications.” Cambridge University Press, 2005.

25. Bhatnagar, P.L., Gross, E.P., and Krook, M. “Model for Collision Processes in Gases. I. Small Amplitude Processes in Charged and Neutral One-Component Systems.” *Physical Review*, 1954, 94, 3, p. 511.

26. He, X., Luo, L.S., “Lattice Boltzmann Model for Incompressible Navier-Stokes Equation”, J*. of Stat. Phys.*, 1997, pp. 927-944

27. Latt, J. “Hydrodynamic limit of lattice Boltzmann equations.” Thèse de doctorat: Univ. Genève, 2007, no. Sc. 3846

28. Bird, R.B., Stewart, W.E., Lightfoot, E.N. “Transport Phenomena.” Second Edition. John Wiley & Sons, 2006.

29. Zou, Q., and He, X. “On pressure and velocity boundary conditions for the lattice Boltzmann BGK model.” *Phys. Fluids*, 1997, 9, p. 1591

30. Gunstensen, A.K. and Rothman, D.H. “Lattice Boltzmann model of immiscible Fluids.” *Phyiscal Review A*, 1991, 43, p. 4320.

31. Swift, M. R., Orlandini, E., Osborn, W. R., Yeomans, J. M., “Lattice Boltzmann Simulation of Nonideal fluids”, *Phys. Rev. E*, 1995, 75, p. 830-833.

32. Shan, X., Chen, H., “Lattice Boltzmann model for simulating flows with multiple phases and components”, *Phys. Rev. E*, 1993, 47, p. 1815-1819

33. Martys, N. & Chen, H. “Simulation of multicomponent fluids in complex three-dimensional geometries by the lattice Boltzmann method.” *Phys. Rev. E*, 1996, 53, p. 743–750.

34. Culligan, K.A., Wildenschild, D., Christensen, B.S.B., Gray, W.G. & Rivers, M.L. “Pore-scale characteristics of multiphase flow in porous media: A comparison of air-water and oil-water experiments.” *Adv. Water Res.,* 2006, 29, p. 227– 238.

35. Sukop, M.C., H.Huang, Lin, C.L., Deo, M.D., Oh, K. & Miller, J.D. “Distributions of multiphase fluid in porous media: Comparison betwwen lattice Boltzmann modeling and micro-X-ray tomography.” *Phys. Rev. E*., 2008, 77, p. 026710.

36. Shan, X. and Doolen, G. “Multi-component lattice-Boltzmann model with interparticle interaction.” *J. Stat. Phys*., 1995, 81, p. 379.

37. Baroud, C.N. and Willaime, H. “Multiphase flow in microfluidics.” *C. R. Physique 5*, 2004, p. 547–555

38. Tan, J., Xu, J.H., Li, S.W., and Luo, G.S. “Drop dispenser in a cross-junction microfluidic device: Scaling and mechanism of break-up.” *Chem. Eng. J.*, 2008, 136, p. 306–311

39. Wu, L. et al. “Numerical simulations of droplet formation in a cross-junction microchannel by the lattice Boltzmann method.” *Int. J. Numer. Meth. Fluids,* 2008, 57, p. 793–810

40. Fox, R.W., McDonald, A.T., and Pritchard, P.J. “Introduction to Fluid Mechanics, Sixth Edition.” John Wiley & Sons, 2004.

41. Lee, W., Walker, L.M., and Anna, S.L. “Role of geometry and fluid properties in droplet and thread formation processes in planar flow focusing.” *Phys. Fluids*, 2009, 21, p. 032103

42. Gu, H., Duits, M.H.G., and Mugele, F. “Droplets Formation and Merging in Two-Phase Flow Microfluidics.” *Int. J. Mol. Sci*., 2011, 12, p. 2572-2597

43. Nisisako, T., Torii, T., and Higuchi, T. “Preparation of picoliter-sized reaction/analysis chambers for droplet-based chemical and biochemical systems.” *Micro Total Analysis Systems*, 2002, pp. 362–364

44. Tice, J., Song, H., Lyon, A., and Ismagilov, R. “Formation of droplets and mixing in multiphase microfluidics at low values of the Reynolds and the capillary numbers.” *Langmuir,* 2003, 19, p. 9127–9133.

45. Dreyfus, R., Tabeling, P., and Willaime, H. “Ordered and discordered patterns in two phase flows in microchannels.” *Phys. Rev. Lett*., 2003, 90, p. 144505.

46. Anna, S.L., Bontoux, N., and Stone, H.A. “Formation of dispersions using ‘flow focusing’ in microchannels.” *Appl. Phys. Lett*., 2003, 82, p. 364

47. Nie, Z. et al. “Emulsification in a microfluidic flow-focusing device: effect of the viscosities of the liquids.” *Microfluid Nanofluid*, 2008, 5, p. 585–594

48. Wu, L. et al. “Three-dimensional lattice Boltzmann simulations of droplet formation in a cross-junction microchannel.” *Int. J. of Multiphase Flow*, 2008, 34, p. 852–864

49. Dupin, M.M., Halliday, I., and Care, C.M. “Simulation of a microfluidic flow-focusing device.” *Phys. Rev. E*, 2006, 73, p. 055701

50. Huang, H. et al. “Proposed approximation for contact angles in Shan-and-Chen-type multicomponent multiphase lattice Boltzmann models.” *Phys. Rev. E*, 2007, 76, p. 066701

51. Parmigiani, A. “Lattice Boltzmann calculations of reactive multiphase flows in porous media.” Thèse de doctorat: Univ. Genève, 2011, no. Sc. 4287

52. Latt, J. et al. “Lattice Boltzmann Modeling of Injection Moulding Process.” *International Conference on Cellular Automata for Research and Industry - ACRI* , 2004, p. 345-354.

53. Shan, X., Yuan, X.F. and Chen, H. “Kinetic theory representation of hydrodynamics: a way beyond the Navier-Stokes equation.” *J. Fluid. Mech.*, 2006, 550, p. 413–441.

54. Stroock, A. et al. “Chaotic Mixer for Microchannels.” *Science, 2002,* 295 p. 647.

55. Song, H. et al. “Experimental test of scaling of mixing by chaotic advection in droplets moving through microfluidic channels.” *Appl. Phys. Lett*., 2003, 83, p. 4664.

56. Gambin, Y. et al. “Ultrafast microfluidic mixer with three-dimensional flow focusing for studies of biochemical kinetics.” *Lab Chip*, 2010, 10, p. 598–609.

57. Taylor, G. “Dispersion of soluble matter in solvent flowing slowly through a tube.” *Proc. R. Soc. Lond. A,* 1953, 219, p. 186-203

58. Stockman, H. “A lattice gas study of retardation and dispersion in fractures: Assessment of errors from desorption kinetics and buoyancy.” *Water Resources Research*, 1997, 33, p. 1823-1831.

59. Li, W. et al. “Simultaneous generation of droplets with different dimensions in parallel integrated microfluidic droplet generators.” *Soft Matter*, 2008, 4, p. 258–262

60. Seo, M. et al. “Microfluidic consecutive flow-focusing droplet generators.” *Soft Matter*, 2007, 3, p. 986–992